

## Original Contributions

---

# A Model of the Ventricular Cardiac Action Potential

## Depolarization, Repolarization, and Their Interaction

Ching-hsing Luo and Yoram Rudy

**A mathematical model of the membrane action potential of the mammalian ventricular cell is introduced. The model is based, whenever possible, on recent single-cell and single-channel data and incorporates the possibility of changing extracellular potassium concentration  $[K]_o$ . The fast sodium current,  $I_{Na}$ , is characterized by fast upstroke velocity ( $V_{max} = 400$  V/sec) and slow recovery from inactivation. The time-independent potassium current,  $I_{K1}$ , includes a negative-slope phase and displays significant crossover phenomenon as  $[K]_o$  is varied. The time-dependent potassium current,  $I_K$ , shows only a minimal degree of crossover. A novel potassium current that activates at plateau potentials is included in the model. The simulated action potential duplicates the experimentally observed effects of changes in  $[K]_o$  on action potential duration and rest potential. Physiological simulations focus on the interaction between depolarization and repolarization (i.e., premature stimulation). Results demonstrate the importance of the slow recovery of  $I_{Na}$  in determining the response of the cell. Simulated responses to periodic stimulation include monotonic Wenckebach patterns and alternans at normal  $[K]_o$ , whereas at low  $[K]_o$  nonmonotonic Wenckebach periodicities, aperiodic patterns, and enhanced supernormal excitability that results in unstable responses ("chaotic activity") are observed. The results are consistent with recent experimental observations, and the model simulations relate these phenomena to the underlying ionic channel kinetics. (Circulation Research 1991;68:1501-1526)**

In the late 1970s, two models of the electrical activity of cardiac cells were formulated based on the formalism introduced by Hodgkin and Huxley.<sup>1</sup> McAllister et al<sup>2</sup> developed a model of the cardiac Purkinje fiber action potential. Subsequently, Beeler and Reuter<sup>3</sup> published a model of the electrical activity of the mammalian ventricular myocyte (referred to as the B-R model in the present paper). The B-R model was based on experimental data that were available at the time from voltage-clamp studies. These data were subject to limitations in available voltage-clamp techniques and their application to multicellular preparations of cardiac muscle.<sup>4</sup> In addition, the concentrations of ions in the extracellular clefts of the multicellular preparations were unknown.

With the development of single-cell and single-channel recording techniques in the 1980s, the limi-

tations of voltage-clamp measurements were overcome and the intracellular and extracellular ionic environments could be controlled. The data from single-channel recordings provide the basis for a quantitative description of channel kinetics and membrane ionic currents. In 1985, DiFrancesco and Noble<sup>5</sup> developed a model of the Purkinje fiber action potential based on available single-cell and single-channel data. Our goal is to incorporate, whenever possible, recent experimental information that have accumulated since the formulation of the B-R model into the formulation of a modified model (referred to as the L-R model in the text) of the mammalian ventricular action potential. The work presented here constitutes the first phase of this effort. In this paper we formulate the fast inward sodium current and the outward potassium currents. We use the model to investigate phenomena that are dominated by these currents and are only minimally influenced by the slow inward current. Therefore, we retain the B-R formulation of the slow inward current to support the plateau of the action potential.

This paper focuses on the depolarization and repolarization phases of the action potential and on phenomena that involve interaction between these processes. These include supernormal excitability,

From the Department of Biomedical Engineering, Case Western Reserve University, Cleveland, Ohio.

Supported by grant HL-33343 from the National Heart, Lung, and Blood Institute, National Institutes of Health, and by a fellowship from the Ministry of Education, Republic of China.

Address for correspondence: Yoram Rudy, PhD, Department of Biomedical Engineering, Case Western Reserve University, Wickenden Building, Room 505, Cleveland, OH 44106.

Received July 10, 1990; accepted January 23, 1991.

Wenckebach periodicity, and aperiodic response of the cell to periodic stimulation. These phenomena were observed recently in single ventricular cells and in Purkinje fibers.<sup>6,7</sup> In the B-R model, the extracellular concentrations of ions are fixed. Because changes in extracellular potassium concentration exert a strong effect on the time course of repolarization,<sup>8,9</sup> we introduce in the model the dependence of the potassium currents on potassium concentration. We also incorporate a negative-slope characteristic of the time-independent potassium current<sup>10,11</sup> and a novel potassium channel that activates at plateau potentials.<sup>12</sup> The fast sodium current is characterized by fast upstroke velocity ( $\dot{V}_{\max}$ )<sup>13</sup> and slow recovery from inactivation,<sup>14</sup> a property that strongly influences the response of the cell to premature stimulation.

In addition to the study of mechanisms that determine the behavior of the single cell, an accurate model of the action potential is important to simulation studies of propagation of excitation in cardiac tissue. Our studies of propagation<sup>15,16</sup> were limited by the inability to simulate important situations of physiological and clinical significance such as the effects of elevated extracellular potassium concentration, an important aspect of ischemia. In addition, our model simulations of reentry<sup>17</sup> demonstrated the importance of the interaction between depolarization and repolarization in the induction and maintenance of reentrant arrhythmias. The need for an accurate representation of this interaction to further elucidate mechanisms underlying abnormal propagation and arrhythmogenesis provided yet another motivation for the development of the action potential model presented here.

### Methods

The general approach is based on a numerical reconstruction of the ventricular action potential by using Hodgkin-Huxley-type formalism.<sup>1</sup> The rate of change of membrane potential (V) is given by

$$\frac{dV}{dt} = -(1/C)(I_i + I_{st}) \quad (1)$$

where C is the membrane capacitance,  $I_{st}$  is a stimulus current, and  $I_i$  is the sum of six ionic currents:  $I_{Na}$ , a fast sodium current;  $I_{si}$ , a slow inward current;  $I_K$ , a time-dependent potassium current;  $I_{K1}$ , a time-independent potassium current;  $I_{Kp}$ , a plateau potassium current; and  $I_b$ , a time-independent background current. The ionic currents are determined by ionic gates, whose gating variables are obtained as a solution to a coupled system of eight nonlinear ordinary differential equations. The ionic currents, in turn, change V, which subsequently affects the ionic gates and currents. The differential equations are of the form

$$\frac{dy}{dt} = (y_* - y)/\tau_y \quad (2)$$

where

$$\tau_y = 1/(\alpha_y + \beta_y)$$

and

$$y_* = \alpha_y/(\alpha_y + \beta_y)$$

y represents any gating variable,  $\tau_y$  is its time constant, and  $y_*$  is the steady-state value of y.  $\alpha_y$  and  $\beta_y$  are voltage-dependent rate constants. In addition,  $\alpha_{K1}$  and  $\beta_{K1}$  of the  $I_{K1}$  channel depend on extracellular potassium concentration.

The integration algorithm used to solve the differential equations is based on the hybrid methods introduced by Rush and Larsen<sup>18</sup> and Victorri et al.<sup>19</sup> Briefly, the algorithm uses an adaptive time step that is always smaller than  $\Delta t_{\max} = 1$  msec. For time intervals of relatively slow changes in V ( $\Delta V \leq \Delta V_{\min} = 0.2$  mV),  $\Delta t$  is set equal to  $\Delta V_{\max}/\dot{V}$ , where  $\Delta V_{\max} = 0.8$  mV. For time intervals of fast changes in V ( $\Delta V \geq \Delta V_{\max}$ ),  $\Delta t$  is set equal to  $\Delta V_{\min}/\dot{V}$ . If this  $\Delta t$  results in  $\Delta V \geq \Delta V_{\max}$ ,  $\Delta t$  is reduced until the condition  $\Delta V < \Delta V_{\max}$  is met. During the stimulus, a fixed time step (0.05 or 0.01 msec) is used to minimize variability in the stimulus duration caused by the time discretization procedure.<sup>20</sup>

Rate constants of ionic gates were obtained by parameter estimation with an adaptive nonlinear least-squares algorithm developed by Dennis et al.<sup>21</sup> All computer programs were coded in FORTRAN 77 (Microsoft, Seattle), and all simulations were implemented (double precision) on a Macintosh IIcx computer.

### Formulation of Equations for Ionic Currents

All ionic currents are computed for 1 cm<sup>2</sup> of membrane. Membrane capacity is set at 1  $\mu\text{F}/\text{cm}^2$ .<sup>22</sup> The formulation is based on experimental data adjusted to 37°C by using a Q<sub>10</sub> adjustment factor. Ionic concentrations for standard preparations are [K]<sub>o</sub>=5.4 mM, [K]<sub>i</sub>=145 mM,<sup>10</sup> [Na]<sub>i</sub>=18 mM,<sup>13,23</sup> [Na]<sub>o</sub>=140 mM, and [Ca]<sub>o</sub>=1.8 mM. [Ca]<sub>i</sub> varies during the action potential; we set [Ca]<sub>i</sub>= $2 \times 10^{-4}$  mM as an initial value under standard conditions. We assume that a short-term stimulation does not appreciably affect the ionic environment of the cell under normal conditions and, therefore, the ionic concentrations (except [Ca]<sub>i</sub>) do not change dynamically in our simulations. The complete set of equations for all ionic currents is provided in Table 1.

$I_{Na}$ : *Fast sodium current.* The model of the fast sodium channel incorporates both a slow process of recovery from inactivation and adequate maximum conductance that results in a realistic rate of membrane depolarization. We adopt the activation (m) and inactivation (h) parameters of Ebihara and Johnson<sup>4</sup> (we refer to the Ebihara-Johnson model of  $I_{Na}$  as the E-J model). The formulation of these parameters is based on data from cardiac cells (chicken embryo) and results in a realistic rate of depolarization ( $\dot{V}_{\max} = 300$  V/sec). However, it does not include the property of slow recovery. Following the methods of Beeler and Reuter,<sup>3</sup> we incorporate a slow inactivation gate (j) to represent this slow process. As suggested by Haas et al.,<sup>24</sup> the steady-

**TABLE 1.** Formulations of Ionic Currents*Inward currents*

## Fast sodium current

$$I_{Na} = 23 \cdot m^3 \cdot h \cdot j \cdot (V - E_{Na})$$

For  $V \geq -40$  mV

$$\alpha_h = \alpha_j = 0.0, \beta_h = 1/(0.13\{1 + \exp[(V + 10.66)/-11.1]\})$$

$$\beta_j = 0.3 \cdot \exp(-2.535 \cdot 10^{-7} V) / \{1 + \exp[-0.1(V + 32)]\}$$

For  $V < -40$  mV

$$\alpha_h = 0.135 \cdot \exp[(80 + V)/-6.8], \beta_h = 3.56 \cdot \exp(0.079V) + 3.1 \cdot 10^5 \cdot \exp(0.35V)$$

$$\alpha_j = [-1.2714 \cdot 10^5 \cdot \exp(0.2444V) - 3.474 \cdot 10^{-5} \cdot \exp(-0.04391V)] \cdot (V + 37.78) / \{1 + \exp[0.311 \cdot (V + 79.23)]\}$$

$$\beta_j = 0.1212 \cdot \exp(-0.01052V) / \{1 + \exp[-0.1378(V + 40.14)]\}$$

For all range of V

$$\alpha_m = 0.32(V + 47.13) / \{1 - \exp[-0.1(V + 47.13)]\}, \beta_m = 0.08 \cdot \exp(-V/11)$$

## Slow inward current

$$I_{si} = 0.09 \cdot d \cdot f \cdot (V - E_{si}), E_{si} = 7.7 - 13.0287 \cdot \ln([Ca]_i)$$

$$\alpha_d = 0.095 \cdot \exp[-0.01(V - 5)] / \{1 + \exp[-0.072(V - 5)]\}$$

$$\beta_d = 0.07 \cdot \exp[-0.017(V + 44)] / \{1 + \exp[0.05(V + 44)]\}$$

$$\alpha_f = 0.012 \cdot \exp[-0.008(V + 28)] / \{1 + \exp[0.15(V + 28)]\}$$

$$\beta_f = 0.0065 \cdot \exp[-0.02(V + 30)] / \{1 + \exp[-0.2(V + 30)]\}$$

$$\text{Calcium uptake: } d([Ca]_i)/dt = -10^{-4} \cdot I_{si} + 0.07(10^{-4} - [Ca]_i)$$

*Outward currents*

## Time-dependent potassium current

$$I_K = \bar{G}_K \cdot X \cdot X_i \cdot (V - E_K), \bar{G}_K = 0.282 \cdot \sqrt{[K]_o/5.4}$$

$$X_i = 2.837 \cdot \{\exp[0.04(V + 77)] - 1\} / \{(V + 77) \cdot \exp[0.04(V + 35)]\} \text{ for } V > -100 \text{ mV and } X_i = 1 \text{ for } V \leq -100 \text{ mV}$$

$$\alpha_X = 0.0005 \cdot \exp[0.083(V + 50)] / \{1 + \exp[0.057(V + 50)]\}$$

$$\beta_X = 0.0013 \cdot \exp[-0.06(V + 20)] / \{1 + \exp[-0.04(V + 20)]\}$$

## Time-independent potassium current

$$I_{K1} = \bar{G}_{K1} \cdot K_{1z} \cdot (V - E_{K1}), \bar{G}_{K1} = 0.6047 \cdot \sqrt{[K]_o/5.4}$$

$$\alpha_{K1} = 1.02 / \{1 + \exp[0.2385 \cdot (V - E_{K1} - 59.215)]\}$$

$$\beta_{K1} = \{0.49124 \cdot \exp[0.08032 \cdot (V - E_{K1} + 5.476)] + \exp[0.06175 \cdot (V - E_{K1} - 594.31)]\} / \{1 + \exp[-0.5143 \cdot (V - E_{K1} + 4.753)]\}$$

## Plateau potassium current

$$I_{Kp} = 0.0183 \cdot K_p \cdot (V - E_{Kp}), E_{Kp} = E_{K1}$$

$$K_p = 1 / \{1 + \exp[(7.488 - V)/5.98]\}$$

## Background current

$$I_b = 0.03921 \cdot (V + 59.87)$$

## Total time-independent potassium current

$$I_{K1(T)} = I_{K1} + I_{Kp} + I_b$$

$I_K$ , time-dependent potassium current ( $\mu A/cm^2$ );  $\bar{I}_K$ , fully activated potassium current ( $\mu A/cm^2$ ) ( $\bar{I}_K = I_K/X$ );  $I_{K1}$ , time-independent potassium current ( $\mu A/cm^2$ );  $I_{Kp}$ , plateau potassium current ( $\mu A/cm^2$ );  $I_b$ , background leakage current ( $\mu A/cm^2$ );  $I_{K1(T)}$ , total time-independent potassium current ( $\mu A/cm^2$ ) ( $I_{K1(T)} = I_{K1} + I_{Kp} + I_b$ );  $I_{Na}$ , fast sodium current ( $\mu A/cm^2$ );  $I_{si}$ , slow inward current ( $\mu A/cm^2$ );  $V$ , membrane potential (mV);  $\dot{V}$ , time derivative of  $V$  (V/sec);  $\dot{V}_{max}$ , maximum rate of rise of  $V$  (V/sec);  $E_i$ , reversal potential of ion  $i$  (mV);  $\bar{G}_i$ , maximum conductance of channel  $i$  ( $mS/cm^2$ );  $[A]_o$ ,  $[A]_i$ , extracellular and intracellular concentrations of ion  $A$ , respectively (mM);  $m$ ,  $h$ ,  $j$ , activation gate, fast inactivation gate, and slow inactivation gate of  $I_{Na}$ ;  $d$ ,  $f$ , activation gate and inactivation gate of  $I_{si}$ ;  $X$ ,  $X_i$ , activation gate and inactivation gate of  $I_K$ ;  $K_1$ , inactivation gate of  $I_{K1}$ ;  $y_z$ , steady-state value of activation (inactivation) gate  $y$ ;  $\alpha_y$ ,  $\beta_y$ , opening and closing rate constants of gate  $y$  ( $msec^{-1}$ );  $\tau_y$ , time constant of gate  $y$  (msec).

state values of  $j$  ( $j_z$ ) are obtained by setting  $j_z = h_z$ , where  $h_z$  is from the E-J model. The time constant of  $j$  ( $\tau_j$ ) is set equal to the  $\tau_j$  of the B-R model. The rate constants  $\alpha_j$  and  $\beta_j$  are obtained by using the parameter estimation procedure mentioned above.<sup>21</sup> The sodium current is

$$I_{Na} = \bar{G}_{Na} \cdot m^3 \cdot h \cdot j \cdot (V - E_{Na}) \quad (3)$$

where  $\bar{G}_{Na}$  is the maximum conductance of the sodium channel ( $23 \text{ mS/cm}^2$ )<sup>4,25</sup>;  $E_{Na}$  is the reversal

potential of sodium [ $E_{Na} = (RT/F) \cdot \ln ([Na]_o/[Na]_i)$ ]; and  $m$ ,  $h$ , and  $j$  are obtained as solutions to Equation 2 with the appropriate rate constants. Note that  $E_{Na}$  computed with the E-J model is 29 mV since  $[Na]_i = 40$  mM in chicken embryo heart cells.<sup>25</sup> In our model we set  $E_{Na} = 54.4$  mV based on  $[Na]_i = 18$  mM in mammalian ventricular cells.<sup>13,23</sup>

$I_{si}$ : Slow inward current. Representation of  $I_{si}$  is the same as in the B-R model. The formulation is provided in Table 1.

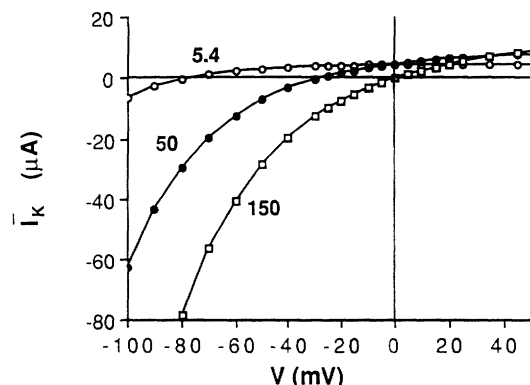


FIGURE 1. Current-voltage ( $I$ - $V$ ) curves of the fully activated time-dependent potassium current ( $I_K$ ) current (denoted  $\bar{I}_K$  in the figure) for  $[K]_o = 5.4, 50$ , and  $150$  mM. Note minimal crossover between curves of different  $[K]_o$  and strong inward rectification.

$I_K$ : Time-dependent potassium current. In patch-clamp experiments, Shibasaki<sup>26</sup> showed that 1) the  $I_K$  channel is controlled by a time-dependent activation gate ( $X$ ) and a time-independent inactivation gate ( $X_i$ ), neither of which depends on  $[K]_o$ ; and 2) the single-channel conductance is proportional to  $\sqrt{[K]_o}$ . We use the equation suggested by Shibasaki:

$$I_K = \bar{G}_K \cdot X \cdot X_i \cdot (V - E_K) \quad (4)$$

and introduce the  $[K]_o$  dependence through

$$\bar{G}_K = 0.282 \cdot \sqrt{[K]_o / 5.4}$$

and

$$E_K = (RT/F) \cdot \ln \left( \frac{[K]_o + PR_{NaK} \cdot [Na]_o}{[K]_i + PR_{NaK} \cdot [Na]_i} \right)$$

where  $PR_{NaK} = 0.01833$  is the Na/K permeability ratio.<sup>27,28</sup> For this value of  $PR_{NaK}$  and  $[K]_o = 5.4$  mM, the computed  $E_K$  is  $-77$  mV, a result that is consistent with the measurements of Beeler and Reuter.<sup>3</sup> Also, note that  $\bar{G}_K = 0.282$  mS/cm<sup>2</sup> for  $[K]_o = 5.4$  mM. This value is obtained from the fully activated current  $\bar{I}_K = I_K/X$  (B-R model,<sup>3</sup> Figure 1) for  $V = -100$  mV, a potential at which  $X_i = 1$ .

$X_i$  introduces the inward rectification property of  $I_K$ . It is obtained from the B-R expression for  $\bar{I}_K$  by factoring out  $\bar{G}_K \cdot (V - E_K)$  at  $[K]_o = 5.4$  mM. The formulation is provided in Table 1. To verify that this formulation correctly introduces the  $[K]_o$  dependence of  $I_K$  we plotted the computed fully activated current ( $\bar{I}_K$ ) for  $[K]_o = 5.4, 50$ , and  $150$  mM (Figure 1). The behavior is consistent with the experimental observations of McDonald and Trautwein,<sup>29</sup> Matsura et al.,<sup>27</sup> and Shibasaki.<sup>26</sup> Note the strong inward rectification and the minimal crossover between curves of different  $[K]_o$ .

$I_{K1}$ : Time-independent potassium current. Sakmann and Trube,<sup>10,11</sup> using patch-clamp techniques, demonstrated two important properties of  $I_{K1}$ : 1) square

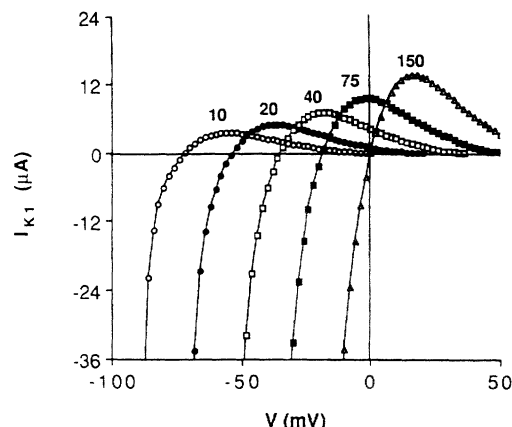


FIGURE 2. Current-voltage ( $I$ - $V$ ) curves of the time-independent potassium current ( $I_{K1}$ ) for different  $[K]_o$  (indicated in the figure in mM). Note the large degree of crossover between curves of different  $[K]_o$ , strong inward rectification, negative slope of the  $I$ - $V$  curves, and zero-current contribution at high potentials.

root dependence of single-channel conductance on  $[K]_o$ ; 2) high selectivity for potassium (i.e.,  $E_{K1} \sim$  Nernst potential of potassium). Kurachi<sup>30</sup> identified an inactivation gate ( $K1$ ) of the  $I_{K1}$  channel. This gate, in addition to its dependence on membrane potential, depends on  $E_{K1}$  and therefore on  $[K]_o$ .  $K1$  closes at high potentials and therefore  $I_{K1}$  has no contribution at this range. In addition, the time constant of  $K1$  is small ( $\tau_{K1} = 0.7$  msec at  $V = -50$  mV for  $[K]_o = 5.4$  mM), so it can be approximated by  $K1_x$  (its steady-state value).

Based on these findings, we formulate the  $I_{K1}$  current as follows:

$$I_{K1} = \bar{G}_{K1} \cdot K1_x \cdot (V - E_{K1}) \quad (5)$$

where

$$E_{K1} = (RT/F) \cdot \ln ([K]_o / [K]_i)$$

$$K1_x = \alpha_{K1} / (\alpha_{K1} + \beta_{K1})$$

$$\bar{G}_{K1} = 0.6047 \cdot \sqrt{[K]_o / 5.4}$$

$$(\bar{G}_{K1} = 0.6047 \text{ at } [K]_o = 5.4 \text{ mM}^{10,31})$$

To verify that this formulation correctly introduces the  $[K]_o$  dependence of  $I_{K1}$  we plotted the computed current-voltage curve for  $[K]_o = 10, 20, 40, 75$ , and  $150$  mM (Figure 2). The results resemble the single-channel measurements of Kurachi (see Figure 12B of Reference 30). Note the strong inward rectification, the crossover between curves of different  $[K]_o$ , the zero contribution at high potentials, and the negative slope over a certain potential range. These characteristics reflect the voltage and  $[K]_o$  dependence of the  $K1$  gate.

It should be emphasized that our definition of  $I_{K1}$  differs from  $I_{K1}$  of the B-R model. The B-R  $I_{K1}$  includes contributions from other currents at plateau potentials. Recently, it was recognized that the current at plateau potentials results from a time-independent,  $[K]_o$ -insensitive channel ( $I_{Kp}$ )<sup>12</sup> and a background current ( $I_b$ ).<sup>32-34</sup> We formulate  $I_{Kp}$  to simulate the behavior of the  $I_{Kp}$  current measured by Yue and Marban<sup>12</sup>:

$$I_{Kp} = \bar{G}_{Kp} \cdot K_p \cdot (V - E_{Kp}) \quad (6)$$

where  $\bar{G}_{Kp} = 0.0183$ ,  $E_{Kp} = E_{K1}$ , and  $K_p = 1/[1 + \exp((7.488 - V)/5.98)]$ . In addition,  $I_b$  is a background current<sup>32-34</sup> that can be formulated as

$$I_b = \bar{G}_b \cdot (V - E_b) \quad (7)$$

where  $\bar{G}_b = 0.03921$  and  $E_b = -59.87$  mV. We define the total time-independent potassium current,  $I_{K1(T)}$ , as

$$I_{K1(T)} = I_{K1} + I_{Kp} + I_b \quad (8)$$

The parameters (conductances, gates, and reversal potentials) of  $I_{K1}$ ,  $I_{Kp}$ , and  $I_b$  are obtained by using a parameter estimation technique<sup>21</sup> to fit the whole-cell  $I_{K1(T)}$  measured by Sakmann and Trube (Figure 4A of Reference 11) for different values of  $[K]_o$ . A comparison of the measured and simulated  $I_{K1(T)}$  is shown in Figure 3 for different values of  $[K]_o$ . Note that the negative slope (which is not a property of the B-R  $I_{K1}$ ) and crossover phenomena are well duplicated by the model. Also, all curves for different values of  $[K]_o$  converge at plateau potentials. This is because  $I_{K1}$ , which depends on  $[K]_o$ , has zero contribution at this potential range, while  $I_{Kp}$  and  $I_b$  are  $[K]_o$  insensitive.

## Results

### Ionic Currents and the Action Potential

The goal of this paper is to investigate, at the ionic channel level, the mechanisms of various electrophysiological phenomena related to depolarization, repolarization, and their interaction. We limit the simulations to phenomena that are dominated by the fast inward sodium current and the outward potassium currents. Figure 4A shows simulated action potentials for different extracellular concentrations of potassium ( $[K]_o = 3, 4, 5.4$ , and  $7$  mM). For the typical physiological concentration of potassium ( $[K]_{o,\text{normal}} = 5.4$  mM), the following characteristics are observed: the threshold potential is at  $-60$  mV, the membrane rate of depolarization ( $V_{\text{max}}$ ) is  $400$  V/sec, the maximum plateau potential is  $17.7$  mV, action potential duration (APD) at  $90\%$  repolarization is  $366$  msec, resting potential is  $-84$  mV, and the overshoot potential is  $41.7$  mV. Note that  $V_{\text{max}}$  is more than three times that of the B-R model ( $V_{\text{max,B-R}} = 115$  V/sec). The fast  $V_{\text{max,L-R}}$  reflects the higher sodium channel conductance in our model and is in good agreement with experimental data from mammalian ventricular cells.<sup>13</sup> Also,  $V_{\text{max,L-R}}$  is faster than that of the E-J model ( $V_{\text{max,E-J}} = 300$  V/sec). This difference results from different reversal potentials for the sodium current ( $E_{Na,L-R} = 54.4$  mV, whereas

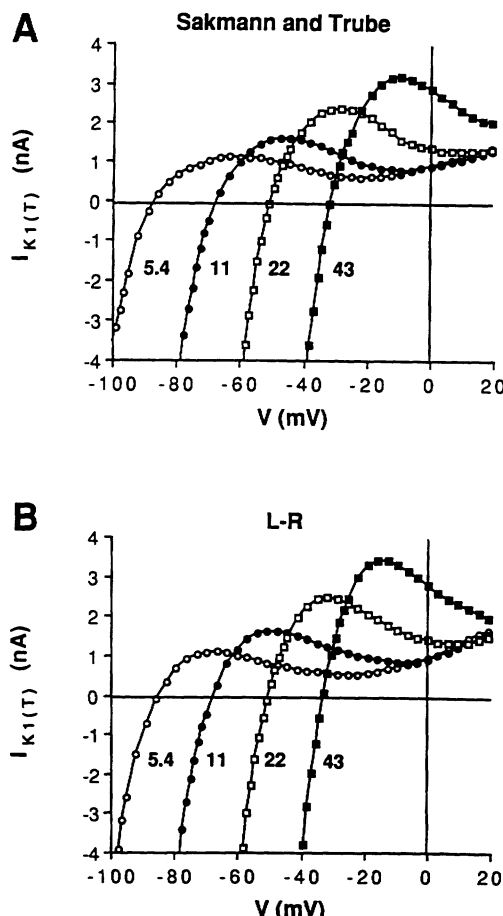


FIGURE 3. Current-voltage ( $I$ - $V$ ) curves of the total time-independent potassium current ( $I_{K1(T)}$ ) for different  $[K]_o$  (indicated in the figure in mM). Panel A: Duplicated from the experimental data of Sakmann and Trube.<sup>11</sup> Panel B: The negative slope, crossover between curves, and overlap of curves at high potentials are well simulated by the present (L-R) model.

$E_{Na,E-J} = 29.0$  mV) and, as a result, greater driving force in the L-R model. The difference in the reversal potential reflects different intracellular concentrations of sodium in the mammalian ventricular cell ( $[Na]_i = 18$  mM) and the chicken embryo ( $[Na]_i = 40$  mM). The overshoot is in good agreement with experimental measurements in guinea pig ventricular cells.<sup>31,35</sup>

The major simulated effects of changes in extracellular potassium concentration are on APD and rest potential ( $V_{\text{rest}}$ ), whereas effects on plateau potentials are minimal. These results are in agreement with experimental observations.<sup>8,9</sup> As  $[K]_o$  increases,  $V_{\text{rest}}$  becomes less negative and APD decreases. For  $[K]_o = 3$  mM,  $V_{\text{rest}}$  is  $-95.5$  mV and APD is  $485$  msec; for  $[K]_o = 7$  mM,  $V_{\text{rest}}$  is  $-78.2$  mV and APD is  $322.6$  msec. For the typical value  $[K]_o = 5.4$  mM, APD is  $366$  msec. This value is in the range of  $305$  msec with a standard deviation of  $55$  msec measured by Isenberg and Klöckner<sup>31</sup> in the guinea pig single ventricular

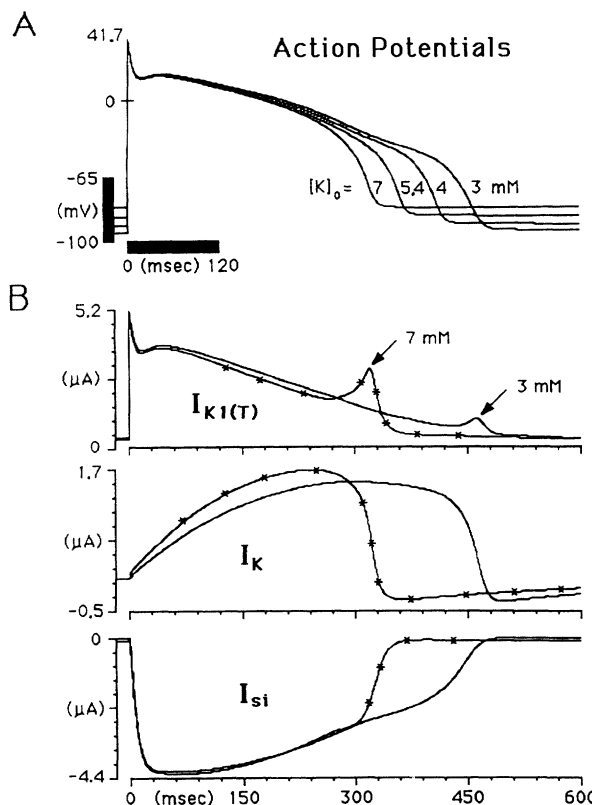


FIGURE 4. Action potentials and ionic currents for  $[K]_o = 7, 5.4, 4$ , and  $3$  mM. Panel A: As  $[K]_o$  decreases, action potential duration increases and resting potential becomes more negative. Panel B: During repolarization the total time-independent potassium current ( $I_{K1(T)}$ ) depends strongly on  $[K]_o$  (arrows), while the time-dependent potassium current ( $I_K$ ) and slow inward current ( $I_{si}$ ) exhibit only weak dependence on  $[K]_o$ .

cell. Figure 4B shows the time course of  $I_{K1(T)}$ ,  $I_K$ , and  $I_{si}$  during the action potential. Note the peak in  $I_{K1(T)}$  during repolarization (arrows). For  $[K]_o = 7$  mM the amplitude of this peak is  $2.87 \mu\text{A}/\text{cm}^2$ , but for  $[K]_o = 3$  mM it is only  $1.0 \mu\text{A}/\text{cm}^2$ . This large difference in  $I_{K1(T)}$  brings about a faster rate of repolarization (1.58 V/sec at 7 mM, 1.1 V/sec at 3 mM) at higher  $[K]_o$ . In addition, the peak of  $I_{K1(T)}$  occurs earlier (at more positive membrane potential), reflecting an increase of the reversal potential  $E_{K1}$ . The result is a shorter APD. Note that  $I_K$  and  $I_{si}$  exhibit only small changes in amplitude during repolarization when  $[K]_o$  is varied (although these currents deactivate earlier in response to the earlier decrease in membrane potential). This is because  $I_{si}$  is independent of  $[K]_o$ , whereas the  $I_K$  dependence on  $[K]_o$  is minimal at plateau potentials (inward rectification, Figure 1). In contrast,  $I_{K1(T)}$  shows strong dependence on  $[K]_o$  at plateau potentials caused by the crossover phenomenon of  $I_{K1}$  (Figure 2). The changes in  $V_{rest}$  parallel changes in the reversal potential of the  $I_{K1}$  current ( $E_{K1}$ ) caused by changes in  $[K]_o$ . In the following sections we use this model of the action potential to

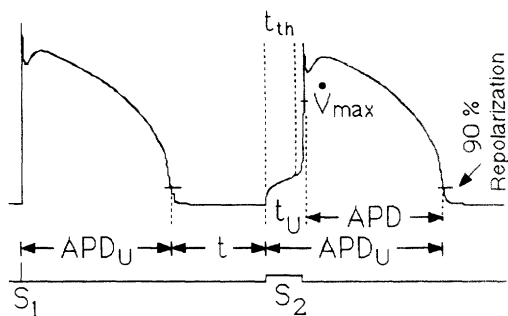


FIGURE 5. The protocol for studying recovery of excitability.  $t$ ,  $t_{th}$ ,  $t_U$ ,  $APD$ , and  $APD_U$  are shown in the figure.  $t$ , Recovery time;  $t_{th}$ , latency from onset of stimulation to threshold potential;  $t_U$ , latency from onset of stimulation to maximum upstroke velocity ( $\dot{V}_{max}$ );  $APD$ , action potential duration from  $\dot{V}_{max}$  to 90% repolarization;  $APD_U$ , action potential duration from onset of stimulation to 90% repolarization, equal to  $APD + t_U$ .  $S_1$  and  $S_2$  are current stimuli.

simulate various physiological phenomena and elucidate their mechanism.

#### Fast Depolarization and Slow Recovery of $I_{Na}$

**Recovery of excitability.** As discussed above,  $I_{Na}$  in the L-R model is characterized by a larger conductance and a faster rate of depolarization (large  $\dot{V}_{max}$ ) than in the B-R model. Also, the L-R model incorporates a fast process of inactivation and a much slower process of recovery from inactivation. In this section we demonstrate the importance of the fast (realistic) rate of depolarization caused by the kinetics of  $I_{Na}$  in determining membrane behavior. Recovery of excitability can be described in terms of  $t_U$  and  $t_{th}$  (defined below) by using the protocol of Figure 5. Test pulses ( $S_2$ )  $1.77 \mu\text{A}$  in amplitude and  $100$  msec in duration are applied at various ( $S_1S_2$ ) intervals from a brief suprathreshold stimulus ( $S_1$ ), which excites a conditioning action potential. Because  $S_1S_2 > APD_U$ ,  $S_2$  is always applied during phase 4 of the action potential. The time from the onset of  $S_2$  to threshold is  $t_{th}$  ( $V = V_{th} \sim -60$  mV). The time from the onset of  $S_2$  to the action potential upstroke as determined from  $\dot{V}_{max}$  is  $t_U$ . As the  $S_1S_2$  interval decreases,  $t_U$  and  $t_{th}$  increase, providing a measure of the excitability of the membrane; the longer  $t_U$  and  $t_{th}$ , the less excitable the membrane.

Figure 6 shows the relation between  $t_U$  and  $t_{th}$  obtained from the protocol of Figure 5. Panel A duplicates the experimental results of Delmar et al (Figure 5B in their paper).<sup>28</sup> Panel B shows the simulated results of the same protocol using the B-R membrane model but with the sodium channel replaced by the L-R formulation. Panels C and D depict simulated results with the original E-J and B-R sodium channel representations, respectively.

The results demonstrate that the experimental behavior (panel A) is duplicated accurately by the L-R and E-J models (panels B and C). However, B-R kinetics of the sodium channel (panel D) causes

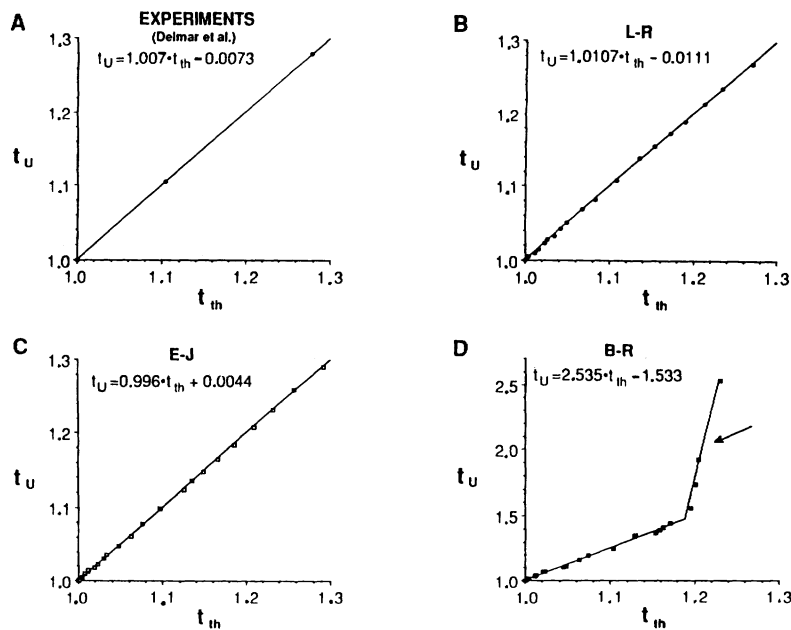


FIGURE 6. The correlation between the latency from onset of stimulation to maximum upstroke velocity ( $t_U$ ) and the latency from onset of stimulation to threshold potential ( $t_{th}$ ). Panel A: Experimental measurements of Delmar et al.<sup>28</sup> Panel B: Present (L-R) model. Panel C: Ebihara-Johnson (E-J) model. Panel D: Beeler-Reuter (B-R) model. Note that the experimental behavior is simulated correctly by the L-R and E-J models that incorporate realistic kinetics of the fast sodium current (fast maximum upstroke velocity), while the B-R model simulation deviates from the experimental behavior, especially for large values of  $t_U$  and  $t_{th}$  (arrow). (Note that  $t_{th}$  is used here for time to threshold and is equivalent to  $t_F$  used by Delmar et al<sup>28</sup>). The  $t_U$  and  $t_{th}$  scales are both normalized to a minimum value of 1.0.

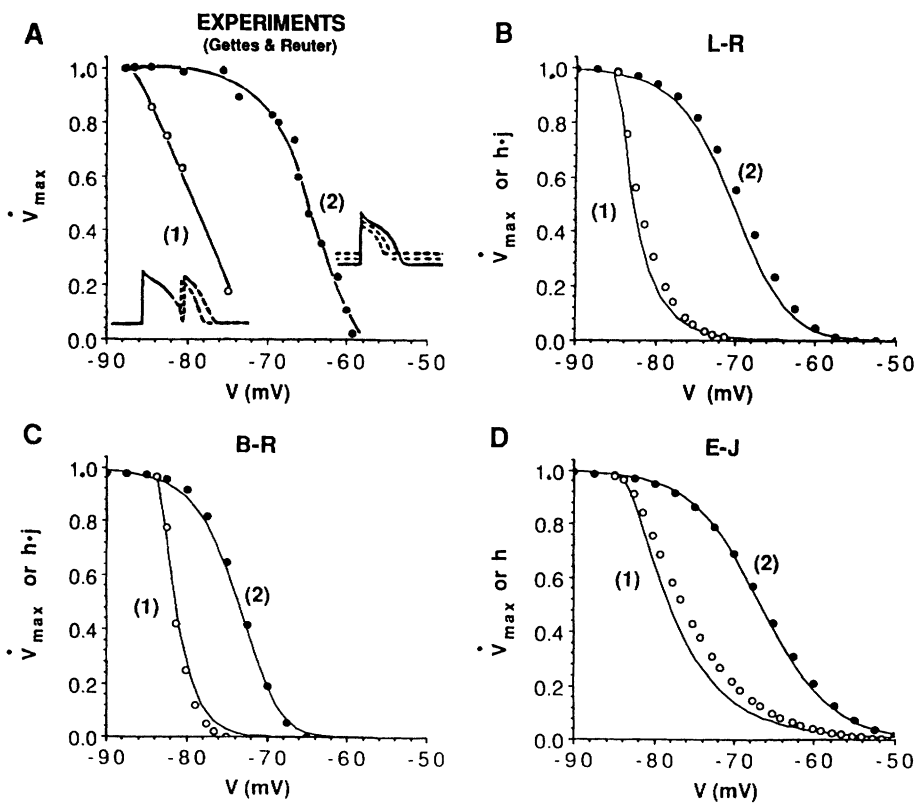
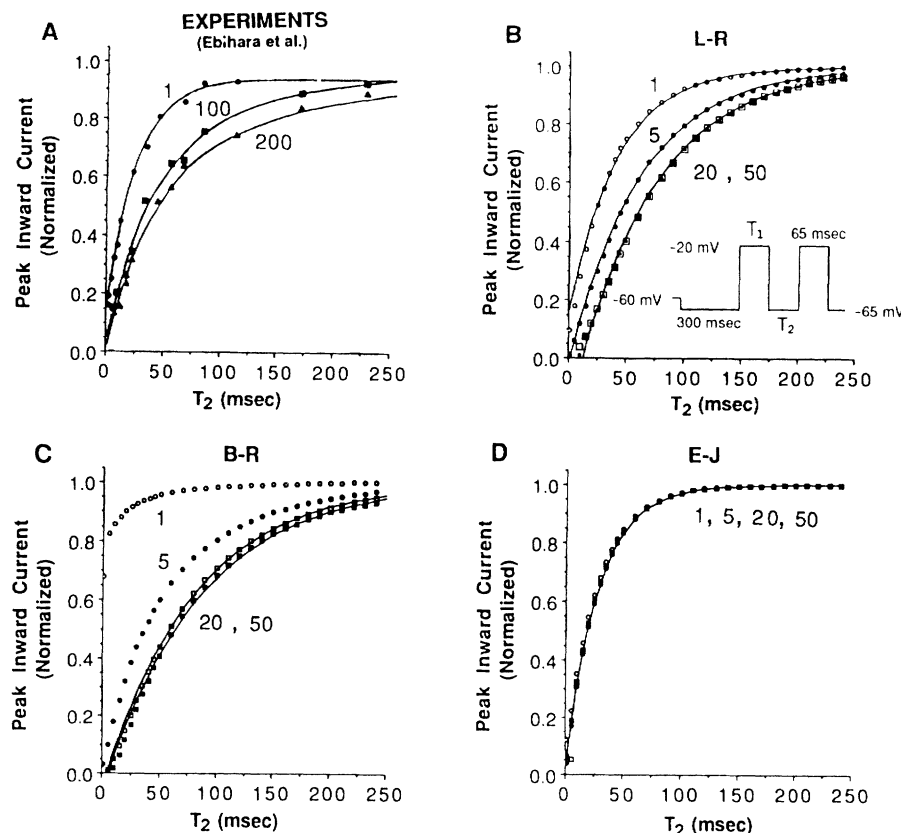
significant deviations from the actual experimental behavior. These include a strong deviation from the linear relation for larger  $t_{th}$  (arrow) and a larger slope (~2.5 times, note different  $t_U$  scale in panel D) of the linear portion for smaller  $t_{th}$ . The slope is close to 1.0 for the L-R and E-J models, duplicating the experimental behavior well and indicating that the increase in  $t_U$  is determined by the increase in  $t_{th}$  (subthreshold response). This is because the latency from threshold potential to  $V_{max}$  is very small (about 2 msec) when the realistic conductance and kinetics of the cardiac sodium channel are incorporated in the model ( $\bar{G}_{Na,B-R}=4$  mS,  $\bar{G}_{Na,L-R}=23$  mS). In contrast, the large slope of the B-R model indicates a significant latency from threshold potential to  $V_{max}$  (greater than 25.5 msec), resulting from the unrealistic conductance and kinetics of the sodium channel in that model.

**Time course of reactivation.** The simulations in this section demonstrate the importance of the slow recovery property of  $I_{Na}$  in determining the membrane reactivation. As mentioned in previous sections, the E-J model does not include the process of slow recovery from inactivation represented by the  $j$  gate. Panel A of Figure 7 duplicates the experimental reactivation data of Ebihara et al (Figure 3 of Reference 36). Panel B shows the results of a simulation with the L-R model. The protocol used both in the experiment and in the model simulations is also illustrated in panel B. Panels C and D are simulations with the B-R and E-J models, respectively. The protocol is as follows: two depolarizing voltage pulses with 45-mV amplitude are applied after preclamping the membrane at -65 mV for 300 msec. The first pulse of duration  $T_1$  inactivates the sodium channel.  $T_2$ , the interval between the depolarizing pulses, is varied to provide different reactivation times before the second test pulse of a constant duration (65

msec) is applied. The membrane response to the second pulse in terms of the peak inward current is plotted as a function of  $T_2$ .

The experimental behavior (panel A) is well duplicated by the L-R model (panel B). The individual curves in panel A are obtained for  $T_1$  in the range 1–200 msec, while in panel B the range is 1–50 msec. This quantitative difference probably reflects the different species (chicken embryo and guinea pig). The B-R model (panel C) deviates from the experimentally observed behavior, especially for  $T_1=1$  msec. As explained below, this is caused by the unrealistic  $I_{Na}$  kinetics of the B-R model. The E-J model (panel D) completely fails to duplicate the dependence on  $T_1$ , and the curves obtained for different  $T_1$  values overlap.

The E-J model (panel D) fails to separate the curves for different  $T_1$  values because slow recovery ( $j$  gate) is not part of this model, so that inactivation and reactivation of the sodium channel are controlled by the fast inactivation  $h$  gate. Because in this model  $h$  is almost completely inactivated in 1 msec when the membrane potential is depolarized to -20 mV ( $\tau_h=0.33$  msec at -20 mV), all curves for  $T_1 \geq 1$  msec overlap. In contrast, the L-R model (panel B) generates different reactivation curves for different values of  $T_1$ , as observed experimentally. This is because the model incorporates a slow inactivation  $j$  gate ( $\tau_j=4.34$  msec at -20 mV). This implies that for  $T_1=1$  and 5 msec the  $j$  gate at the end of  $T_1$  is inactivated to a different degree, resulting in different reactivation curves. For  $T_1 \geq 20$  msec, the  $j$  gate is completely inactivated at a membrane potential of -20 mV, and all the curves overlap. In addition, since for  $T_1 > 1$  msec the recovery process is controlled by the  $j$  gate, all reactivation curves can be fit by a single exponential. In particular, for  $T_1 \geq 20$  msec all curves are represented by the same time constant



( $\tau=70$  msec), which is very close to the  $\tau_j$  value at  $V=-65$  mV ( $\tau_j=77.4$  msec), as expected.

**Membrane responsiveness.** This simulation demonstrates the importance of the slow inactivation  $j$  gate in determining the membrane response during the repolarization phase of an action potential. Results are shown in Figure 8. Panel A is the experimental data of Gettes and Reuter (Figure 7 of Reference 14). Panels B, C, and D are the L-R, B-R, and E-J models, respectively. The protocols are illustrated in panel A. Curve 1 is obtained from protocol 1 by applying a suprathreshold stimulus that scans the repolarization phase of an action potential. Curve 2 is obtained from protocol 2 by stimulating the membrane after 500 msec of preclamping at different potential levels. For both curves  $\dot{V}_{max}$  is shown (discrete points) as a function of the membrane potential at the onset of the stimulus. In panels B-D the solid curves are  $h \cdot j$  (or only  $h$  for the E-J model) computed for the same protocols.

By using protocol 1, the range of membrane potential over which  $\dot{V}_{max}$  drops from its maximum value to 0.2 of the maximum is well simulated by the L-R and B-R models. This normalized value (0.2) is obtained experimentally (panel A, curve 1) for a membrane potential of  $-76$  mV. The corresponding simulated values are  $-78$  mV for both models. In contrast, curve 1 in the E-J model (panel D) is shifted to less negative potentials. This is because the E-J model does not incorporate a slow recovery process of the sodium channel. An equivalent statement is that in the E-J model  $j$  is always 1. However, the L-R and B-R models incorporate a slow recovery  $j$  gate that is not fully recovered during the repolarization phase, shifting the curve to a more negative range of membrane potentials.

Curve 2 reflects steady-state behavior of the membrane since the stimulus was applied after a long (500-msec) preconditioning period. The L-R model correctly simulates the behavior of  $\dot{V}_{max}$  for these conditions (compare curve 2 in panels B and A). In contrast, a shift of curve 2 to more negative potentials is observed in the B-R model (panel C). This difference reflects the different characteristics of  $h_s$  and  $j_s$  in the two models.

Note that the  $\dot{V}_{max}$  behavior is closely approximated by the  $h \cdot j$  curves (deviations are caused by currents other than  $I_{Na}$ ). This implies that the membrane responsiveness is controlled by the  $h$  and  $j$  gates (because of its fast time constant,  $m$  obtains its maximum value of 1 within 0.2 msec and its effect is negligible). Because curve 2 is obtained under steady-state conditions, it is closely approximated by  $h_s \cdot j_s$ . The difference between curves 1 and 2 results from the fact that during repolarization (curve 1)  $h$  and  $j$  do not reach their steady-state values. The E-J model does not incorporate a  $j$  gate. Therefore, the difference between curves 1 and 2 in panel D implies that the rate of repolarization is too fast for  $h$  to reach steady state. Of course, the same is true for the much slower  $j$  gate. Since during repolarization  $j$  is

almost completely inactivated and since  $\tau_j > > \tau_h$ , it follows that the membrane responsiveness is mostly determined by the  $j$  gate.

#### Supernormal Excitability

Supernormality, which can be defined as greater than normal excitability during or immediately after the action potential repolarization phase, is a known property of cardiac preparations at low extracellular potassium concentrations.<sup>7,37-39</sup> The strength-interval curve, used to investigate supernormality, is obtained from the protocol shown in Figure 5 by applying a test pulse,  $S_2$ , after an action potential excited by a stimulus,  $S_1$ . By varying the  $S_1S_2$  interval and the current amplitude of  $S_2$ , the threshold current ( $I_{th}$ ) is obtained as a function of the  $S_1S_2$  interval. Based on such excitability measurements, Spear and Moore<sup>39</sup> found that 1) supernormality disappears when  $[K]_o$  is elevated above 5 mM and 2) the supernormal period at fixed  $[K]_o$  is independent of the APD and is determined by the characteristics of the membrane potential during repolarization.  $I_{K1}$  and  $I_K$  of the L-R model can change their reversal potentials and conductances in response to variations in  $[K]_o$ . We used the L-R model to simulate and investigate supernormality. Figure 9 shows the simulated strength-interval curves for  $[K]_o=7, 4.6, 4$ , and 3 mM, covering late phase 3 and early phase 4 of the action potential. The simulated protocol followed the experimental protocol described above (also see Figure 5).  $I_{th}$  is defined as the critical current amplitude for which the peak sodium current is greater than 4  $\mu$ A (1% of the maximum current for a fully recovered membrane and suprathreshold stimulus). Note that test stimuli of very short duration ( $T=0.5$  msec) were used to investigate the instantaneous membrane excitability at that  $S_1S_2$  interval. The abscissa is normalized by setting the 70% repolarization of the action potential as time zero. Clearly, supernormality is observed for  $[K]_o \leq 4.6$  mM (but not for  $[K]_o=7$  or 5.4 mM) as a notch (local minimum followed by a local maximum) in the strength-interval curve. With decreasing  $[K]_o$ , the peak-to-peak amplitude of the notch increases and so does the width of the "supernormal window." This time window is defined as the interval during which the threshold is lower than the local maximum that follows the notch. The supernormal window is indicated in the figures by two broken vertical lines.

Plotting  $I_{th}$  versus the potential difference ( $\Delta V = V_{th} - V$ ) for the membrane to reach the threshold potential ( $V_{th}$ ), the linear relation of Figure 10 is obtained for all values of  $[K]_o$ . This linear relation implies that the membrane response during repolarization can be characterized in terms of the membrane potential and the threshold potential for all values of  $[K]_o$ . It also implies that the threshold current does not depend on APD, as observed experimentally by Spear and Moore.<sup>39</sup>

To explain the underlying mechanism of supernormality in terms of membrane channel kinetics, the

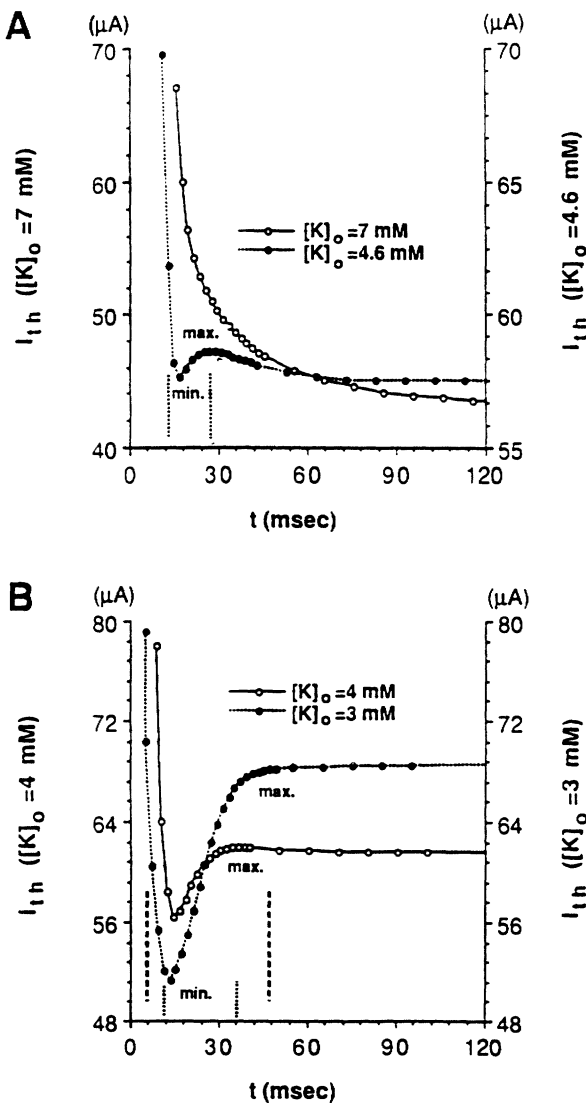


FIGURE 9. Strength-interval curves ( $I_{th}$ ) for  $[K]_o = 7, 4.6, 4$ , and  $3 \text{ mM}$  are plotted as a function of recovery time  $t$ . Time zero ( $t=0$ ) is set at 70% repolarization. Panel A:  $[K]_o = 7$  and  $4.6 \text{ mM}$ . Panel B:  $[K]_o = 4$  and  $3 \text{ mM}$ . max and min, Local maximum and minimum of  $I_{th}$ , respectively. The supernormal window (represented by two vertical broken lines for each curve) is defined as the time interval during which  $I_{th}$  is smaller than the local maximum.

following simulation was carried out for  $[K]_o = 7 \text{ mM}$ . The  $j$  gate of the sodium channel was clamped at the value of 1 for all times and the strength-interval curve was computed (Figure 11A). The unclamped strength-interval curve is also plotted for comparison. With  $j=1$ , sodium channel recovery from inactivation is controlled by the  $h$  gate and its much faster kinetics ( $\tau_h < \tau_j$ ). Under these conditions, supernormality is observed in Figure 11A even for  $[K]_o = 7 \text{ mM}$ . In contrast, when  $j$  is free to vary according to its normal kinetics, no supernormality is observed for this concentration of  $K_o$ , in agreement with the experimental behavior.<sup>7,39</sup> In Figure 11B,  $V$  and  $V_{th}$

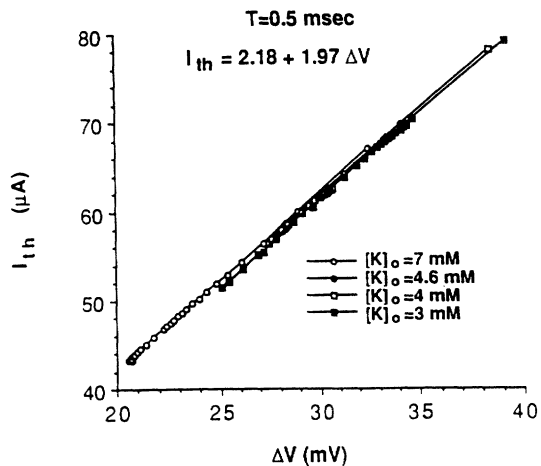


FIGURE 10. The relation between threshold current ( $I_{th}$ ) and change in membrane potential ( $\Delta V = V_{th} - V$ ) for a brief stimulus of 0.5-msec duration. The linear relation is described by  $I_{th} = 2.18 + 1.97 \cdot \Delta V$  and is independent of  $[K]_o$ .

are plotted as a function of time during repolarization. The curve for  $V$  is the same for both  $j=1$  and  $j$ -unclamped conditions (because the sodium channel does not contribute to  $V$  during repolarization). On the other hand, the  $V_{th}$  curve is influenced by the  $j$  gate kinetics. For the clamped condition ( $j=1$ )  $V_{th}$  decreases earlier in time, reflecting faster recovery of membrane excitability. Also, the value of  $V_{th}$  just after the absolute refractory period (arrows) is larger, followed by a steep decrease (approximately 3.5 V/sec) over a period of 6 msec. During the same interval, the membrane potential drops at a rate of about 1.33 V/sec. This implies that  $\Delta V$  (defined as  $V_{th} - V$ ) is decreasing rapidly during this interval, bringing about a proportional decrease in  $I_{th}$  (Figure 10) that constitutes the descending portion of the notch in the strength-interval curve (Figure 11A, DES). Beyond this interval, the membrane potential drops faster than  $V_{th}$ , increasing  $\Delta V$  and, therefore,  $I_{th}$  (ascending portion of the notch, ASC in Figure 11A). This nonmonotonic behavior of  $\Delta V$  is the basis for the notch in the strength-interval curve and, hence, for supernormality. For larger values of  $t$ , both  $V_{th}$  and  $V$  approach their steady-state values with  $\Delta V$  (and hence  $I_{th}$ ) approaching a constant. When the  $j$  gate is free to vary according to its normal kinetics ( $j$ -unclamped in Figure 11B), the  $V_{th}$  curve is shifted to the right toward later times. As a result, the drop in the  $V_{th}$  curve occurs over an interval during which  $V$  decreases slowly and, in particular, always slower than  $V_{th}$  (0.5 and 1.4 V/sec, respectively). Consequently,  $\Delta V$  (and  $I_{th}$ ) is monotonically decreasing ( $j$ -unclamped in Figure 11A), and no supernormality is observed. It is clear that the nonmonotonic, supernormal behavior is determined by the shape of the  $V_{th}$  curve, which in turn is determined by the recovery of the sodium channel. As will be explained below, the sodium channel recovers faster at low  $[K]_o$ ,

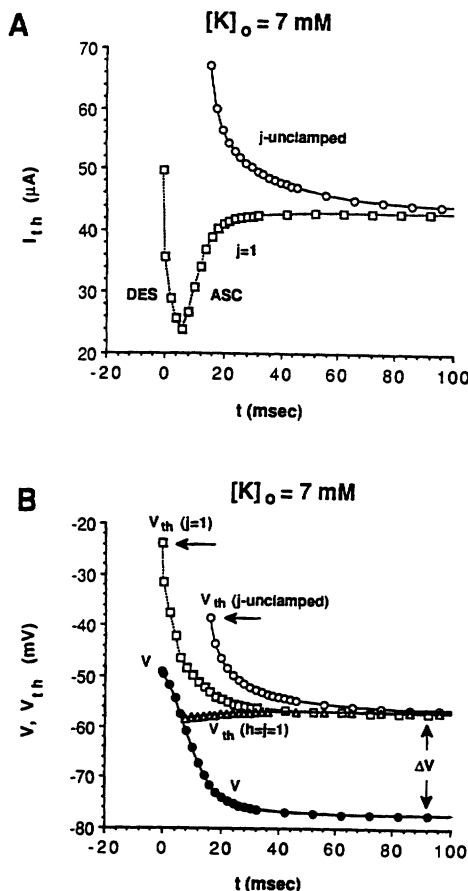


FIGURE 11. Panel A: Strength-interval curves ( $I_{th}$ ) for  $[K]_o = 7 \text{ mM}$ . Two conditions are shown:  $j$  clamped at the value of 1 ( $j=1$ ) and  $j$  free to vary ( $j$ -unclamped). DES and ASC, descending and ascending portions, respectively, of the notch in the strength-interval curve. Panel B: Threshold potential ( $V_{th}$ ) and membrane potential ( $V$ ) during repolarization for  $[K]_o = 7 \text{ mM}$ .  $V_{th}$  is shown for three conditions:  $j=1$ ,  $h=j=1$ , and  $j$ -unclamped.  $V$  for all three conditions is the same. In both panels  $t$  is the recovery time from 70% repolarization.

creating the possibility of a supernormal phase when  $[K]_o \leq 4.6 \text{ mM}$ .

A clear demonstration of the dominant effect of the sodium recovery process on the  $V_{th}$  curve is provided in Figure 11B. When both the  $h$  gate and  $j$  gate are clamped at the value of 1,  $V_{th}$  is constant, except for a small decrease (for  $t < 30 \text{ msec}$ ) caused by  $I_{si}$  (this decrease in  $V_{th}$  disappears when we set  $I_{si}=0$  during the stimulation). The threshold potential is also affected by  $I_{KI(T)}$  and  $I_K$ ; however, the contribution is very small.

Figure 12 shows  $V$  and  $V_{th}$  as a function of time for different  $[K]_o$  in the range of 3–7 mM ( $j$  is free to vary according to its normal kinetics). As  $[K]_o$  decreases from 7 to 3 mM, the resting membrane potential changes from  $-78.2$  to  $-95.5 \text{ mV}$  (Figure 12A), resulting in a decrease of  $\tau_j$  from 33 to 7 msec during late phase 3 and phase 4 of the action potential (arrows in Figure 12A). Therefore, the sodium chan-

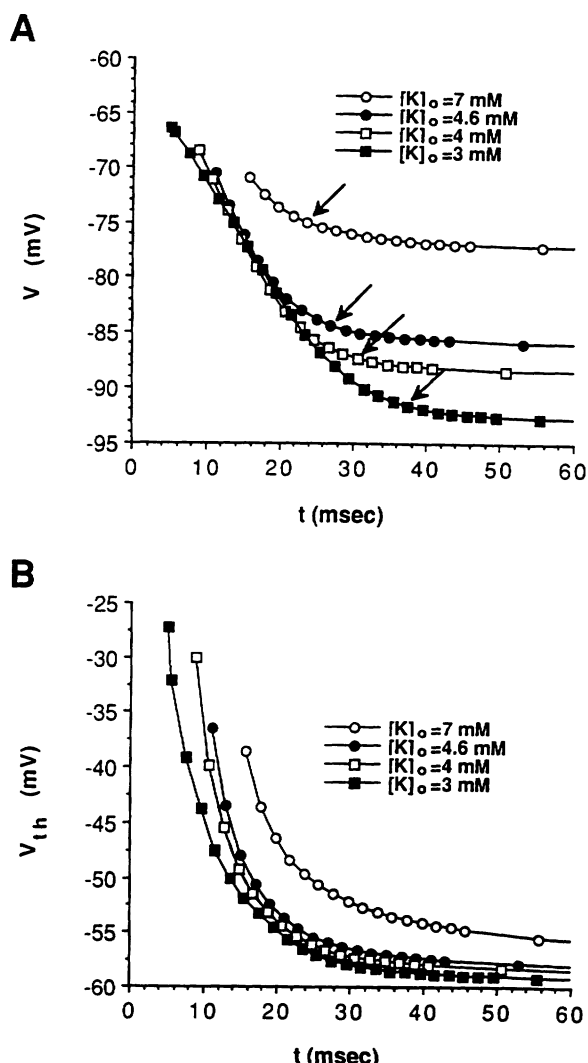


FIGURE 12. Membrane potential ( $V$ , panel A) and threshold potential ( $V_{th}$ , panel B) are plotted as a function of recovery time ( $t$ ) for different  $[K]_o$ . As  $[K]_o$  decreases, membrane potential reaches the resting value later in time (arrows), while threshold potential decreases earlier in time. This increases the width and amplitude of the supernormal notch shown in Figure 9.

nel recovers earlier for lower  $[K]_o$  (Figure 12B) during a phase of fast decrease of  $V$ . As a result, a phase is created during which  $V$  decreases faster than  $V_{th}$ . In addition, the membrane potential reaches a phase of very slow decrease (i.e., end of ascending portion of the supernormal notch) later in time for lower  $[K]_o$  (arrows in Figure 12A). The result of these two effects is the appearance of a supernormal window for  $[K]_o \leq 4.6 \text{ mM}$  and a widening of this window as  $[K]_o$  is further decreased (Figure 9). The peak-to-peak amplitude of the supernormal notch also increases when  $[K]_o$  is decreased. This is because the local minimum (see Figure 9) decreases, reflecting a smaller  $\Delta V$  caused by the faster decrease of  $V_{th}$  for lower  $[K]_o$  (Figure 12B). Also, the local maximum following the notch increases with decreas-

ing  $[K]_o$ , reflecting a larger  $\Delta V$  caused by more negative rest potentials.

It should be emphasized that the E-J representation of the sodium channel does not include a slow inactivation  $j$  gate. Therefore, the E-J strength-interval curves are similar to the strength-interval curves obtained by the L-R model with  $j=1$ . As shown above (Figure 11A), under these conditions, supernormality is a property of the model even for high extracellular concentrations ( $[K]_o=7$  mM) in contradiction to experimental observations.<sup>7,39</sup> This, of course, is a nonphysiological behavior that results from a nonphysiological fast recovery of the sodium channel.

The simulations described above were performed with a test stimulus,  $S_2$ , of 0.5-msec duration. Experimentally, Chialvo et al<sup>7</sup> used a stimulus of 20 msec. Our choice of a short stimulus was dictated by the resolution needed for scanning the supernormal window whose minimum duration is 12 msec. Also, we were interested in determining instantaneous membrane excitability without the influence of a long stimulus duration. To investigate the effects of the stimulus duration ( $T$ ) on membrane excitability, we redefine the strength-interval curve in terms of threshold charge introduced by the stimulus ( $Q_{th}=I_{th} \cdot T$ , Figure 13). In Figure 13A,  $Q_{th}$  is plotted for an interval of 80 msec that includes the supernormal phase. Stimuli of two durations ( $T=0.5$  and 20 msec) are compared. For  $T=20$  msec,  $Q_{th}$  is larger (note different scales), the amplitude of the supernormal notch is twice as large, and the notch is shifted toward earlier time. Figure 13B covers a later time interval that includes late phase 4 of the action potential. During this time interval, the behavior of  $Q_{th}$  for  $T=0.5$  and 20 msec is very different. For  $T=0.5$  msec,  $Q_{th}$  displays a very small and slow increase, while for  $T=20$  msec,  $Q_{th}$  displays a relatively large decrease. It should be commented that similar results were obtained for all  $[K]_o$  values, except no supernormality was observed for  $[K]_o>4.6$  mM ( $[K]_o=4$  mM is shown here as an example).

Figure 14 provides an explanation for these differences between strength-interval curves constructed with stimuli of different durations. Figure 14A shows the total charge ( $Q_{total}$ ) carried by all ionic channels during critical subthreshold stimuli for a short ( $T=0.5$  msec) and a long ( $T=20$  msec) stimulus duration (note the different scales). For both durations,  $Q_{total}$  is positive, indicating a net positive charge leaving the cell. For  $T=0.5$  msec,  $Q_{total}$  is negligible compared with the stimulus charge  $Q_{th}$  (Figure 13). However, for  $T=20$  msec,  $Q_{total}$  is about half the magnitude of  $Q_{th}$  (Figure 13, note the different scales). This significant amount of charge that is lost to the extracellular medium during a long stimulus is the basis for the difference between the strength-interval curves of Figure 13. The  $Q_{th}$  supplied by a very short stimulus can be regarded as the amount of charge needed to bring the membrane to threshold with minimal charge losses to the extracellular me-

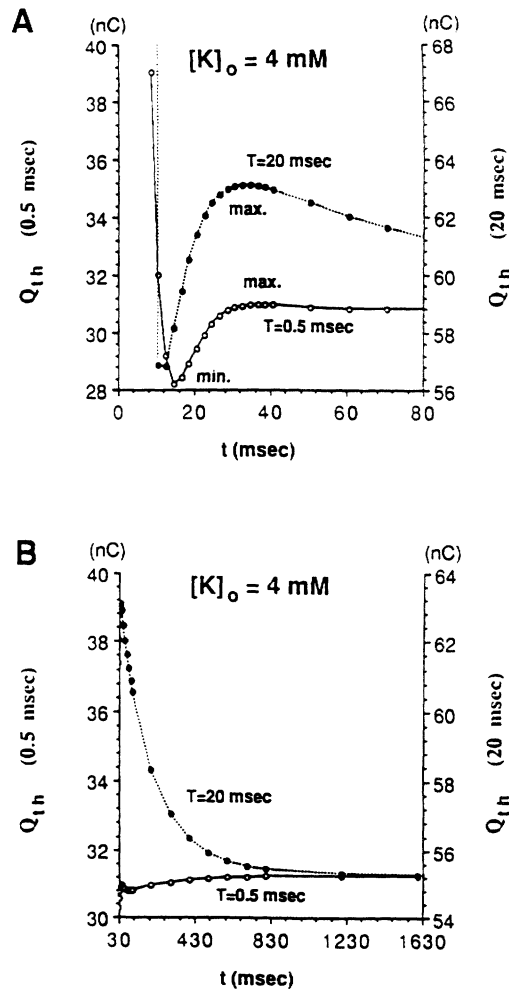


FIGURE 13. Threshold charge  $Q_{th}=I_{th} \cdot T$  ( $I_{th}$  is threshold current and  $T$  is stimulus duration) for  $[K]_o=4$  mM and two different stimulus durations ( $T=0.5$  and 20 msec). Panel A: Time interval (0–80 msec) covering the supernormal phase. Note that the peak-to-peak amplitude of the supernormal notch is about twice larger for  $T=20$  msec than for  $T=0.5$  msec. Panel B: Phase 4 of an action potential. As time increases,  $Q_{th}$  decreases significantly for  $T=20$  msec but is almost constant for  $T=0.5$  msec.

dium. In contrast, the  $Q_{th}$  supplied by a long stimulus can be divided into two components:  $Q_{th}$  supplied by a very short stimulus and the total charge ( $Q_{total}$ ) lost to the extracellular medium during the duration of the stimulus. The fact that  $Q_{th}$  includes  $Q_{total}$  explains the large values of  $Q_{th}$ , including the large amplitude of the maximum that follows the supernormal notch (Figure 13A) when a long stimulus duration is used. Figure 14B shows the contributions of the different ionic channels to  $Q_{total}$  for a stimulus of 20 msec applied at different times,  $t$ , during phase 3 to phase 4 of an action potential. For large  $t$ , all contributions except  $Q_{K1(T)}$  approach very small values, identifying  $I_{K1(T)}$  as the reason for the large rheobase needed when long stimuli are used (Figure 13B). During phase 3 ( $t<20$  msec), a large decrease in  $Q_{total}$  from

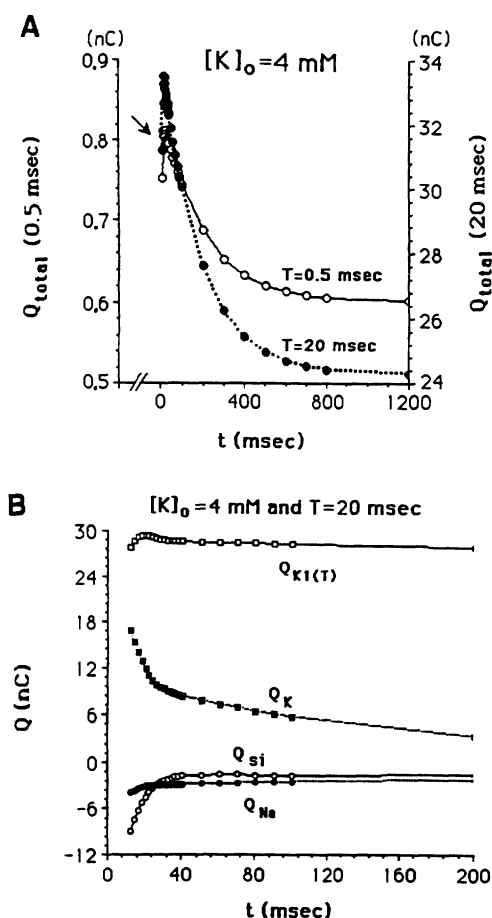


FIGURE 14. Total charge ( $Q_{\text{total}}$ ) lost to the extracellular medium during the duration of stimulation ( $[K]_o = 4 \text{ mM}$ ). Panel A: For short duration ( $T=0.5 \text{ msec}$ ),  $Q_{\text{total}}$  (left ordinate) is negligible in comparison to threshold charge ( $Q_{\text{th}}$ ) in Figure 13, while for long duration ( $T=20 \text{ msec}$ ),  $Q_{\text{total}}$  (right ordinate) is significant (note scale difference). Panel B: The contribution of each ionic channel to  $Q_{\text{total}}$  for  $T=20 \text{ msec}$ : 1) the total time-independent potassium current charge ( $Q_{K_{1(T)}}$ ) elevates the rheobase threshold charge at all phases, 2) the decay of time-dependent potassium current charge ( $Q_K$ ) reflects the deactivation kinetics of the time-dependent potassium current activation gate, and 3) the slow inward current contributes at late phase 3 and early phase 4 because of incomplete inactivation.  $Q_{si}$ , slow inward current charge;  $Q_{Na}$ , sodium current charge.

its peak value is observed as the 20-msec stimulus is applied earlier in time (Figure 14A, arrow). This is caused by an increase in the magnitude of (the negative)  $Q_{si}$  and a decrease of  $Q_{K_{1(T)}}$  as  $t$  decreases (Figure 14B).  $Q_{si}$  increases since, for a small  $t$ , the stimulus is applied during a phase when  $I_{si}$  is not completely inactivated.  $Q_{K_{1(T)}}$  decreases because the stimulus is applied during the negative slope phase of  $I_{K1}$ . This additional contribution of 2.3 nanocoulombs to the decrease in  $Q_{\text{th}}$  is a substantial fraction of the amplitude of the supernormal notch (6 nC). The result is a supernormal notch of about twice the amplitude as compared with that for a 0.5-msec

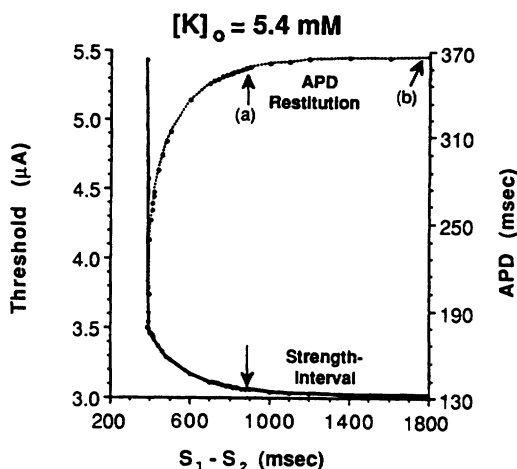


FIGURE 15. Strength-interval curve and action potential duration (APD) restitution curve for  $[K]_o = 5.4 \text{ mM}$  and  $T=20 \text{ msec}$ . Lower arrow indicates the stimulus strength (3.06  $\mu\text{A}$ ) used to study rate-dependent block. See text for definitions of a and b.

stimulus (Figure 13A). The relatively fast decrease of  $Q_{\text{th}}$  during phase 4 ( $t=30-450 \text{ msec}$  in Figure 13B,  $T=20 \text{ msec}$ ), when long stimuli are used, reflects a similar behavior of  $Q_K$  (Figure 14B). Note that contributions from all other currents are constant during this phase; in particular,  $Q_{K_{1(T)}}$  is constant since  $I_{K_{1(T)}}$  is time independent and the membrane potential during this phase is almost constant. Therefore, for long stimuli, the membrane excitability during phase 4 is determined by the kinetics of  $I_K$  (the time-dependent X gate). In contrast,  $Q_{\text{th}}$  is almost constant over the entire phase 4 when short stimuli are used (Figure 13B,  $T=0.5 \text{ msec}$ ). This is because for short stimuli  $Q_{\text{th}}$  is determined by  $V_{\text{th}}$  and  $V$  (negligible contribution from  $Q_{\text{total}}$ ), which do not change significantly during phase 4. As will become clear in the next section, the behavior of the strength-interval curve during phase 4 strongly influences the response of the cell to repetitive stimulation. For short stimulus duration one expects minimal dependence of the response on the timing of stimulation during phase 4 (constant excitability, Figure 13B,  $T=0.5 \text{ msec}$ ). In contrast, for long stimuli, the response is strongly influenced by the timing (Figure 13B,  $T=20 \text{ msec}$ ). This implies that to investigate rate-dependent response patterns (e.g., Wenckebach periodicity), stimuli of long duration should be used.

#### Wenckebach Periodicity and Channel Behavior

Wenckebach periodicity is defined as a periodic, rate-dependent activation failure in cardiac tissue. Recently, this phenomenon was observed in isolated guinea pig<sup>6</sup> or rabbit<sup>40</sup> ventricular myocytes and in sheep cardiac Purkinje fibers.<sup>7</sup> In this section we study the Wenckebach phenomenon by simulating periodic pacing of single myocytes with the use of the L-R membrane model. The response of the membrane to periodic stimulation can be analyzed in terms of the strength-interval curve and the APD

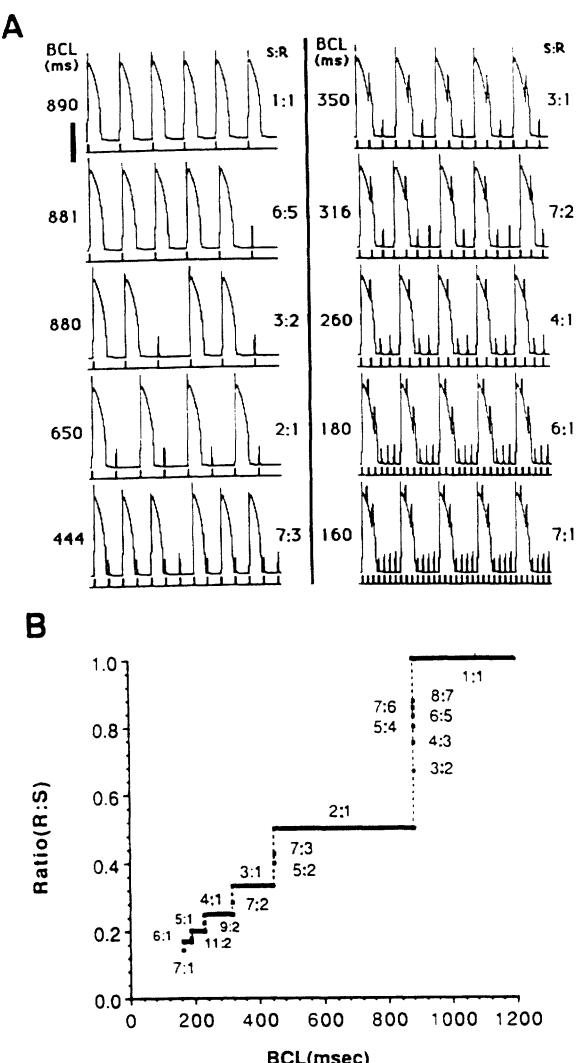


FIGURE 16. Periodic rate-dependent patterns for normal  $[K]_o=5.4$  mM. Panel A: Examples of activation patterns (calibration bar, 52.5 mV). Numbers on the left indicate basic cycle length (BCL), whereas ratios on the right are the resulting stimulus-to-response (S:R) patterns. The train of stimuli is indicated below each pattern. Panel B: The staircase plot of response-to-stimulus (R:S) ratios as a function of BCL. The numbers inside the panel indicate the S:R ratios.

restitution curve. During phases 3 and 4 of an action potential, the strength-interval curve describes the recovery of membrane excitability, whereas the restitution curve describes the recovery of APD of premature responses.<sup>41,42</sup> The simulated strength-interval and APD restitution curves for  $[K]_o=5.4$  mM are shown in Figure 15. Both curves display a monotonic behavior that is determined by the time course of deactivation of the  $I_K$  X gate. In the following simulations, a stimulus strength of  $3.06 \mu\text{A}$  that corresponds to threshold stimulation at  $S_1S_2=882$  msec was used (indicated by the lower arrow in Figure 15). Stimulus duration of 20 msec was used for reasons described above (conclusion of previous sec-

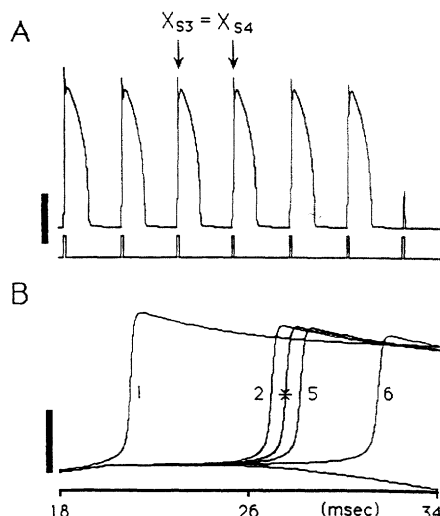


FIGURE 17. Rate-dependent block is studied by resetting the activation ( $X$ ) gate of the time-dependent potassium current value at onset of stimulation ( $X_s$ ). Panel A: Stimulus-to-response (S:R) ratio of 6:5 changes to 7:6 by setting  $X_{S4}=X_{S3}$ . The train of stimuli is shown below the pattern. Panel B: The action potentials for the pattern in panel A are redrawn with the onset of stimulation for all beats set at time zero. The superimposed third and fourth action potentials (indicated by \*) clearly indicate that beat 4 is exactly the same as beat 3 because of their equal values of  $X_s$ . Calibration bars for action potentials are 35 mV in both panels.

tion) and to be consistent with the experimental protocols of Chialvo et al.<sup>7</sup> and Delmar et al.<sup>6</sup> Stimulation was applied at a basic cycle length (BCL) ranging from 160 to 2,000 msec. Simulated activation patterns for different BCLs are shown in Figure 16A. A staircase plot of response-to-stimulus (R:S) ratios versus BCL is shown in Figure 16B (numbers in the figure indicate stimulus-to-response [S:R] ratios). The staircase pattern demonstrates phase-locking at S:R ratios of integer values (1:1, 2:1, 3:1, etc.) and sharp transitions between these values through many noninteger S:R ratios. This pattern is in good agreement with the experimental observations of Chialvo et al.<sup>7</sup> To elucidate the underlying mechanism of the Wenckebach phenomenon observed in single cells the following simulations were performed.

As we discussed in the previous section, the post-refractory period (phase 4 of an action potential) is dominated by the X gate of  $I_K$ .<sup>6,28</sup> Therefore, the Wenckebach phenomenon is likely to be related to the value of X just before the stimulation is applied ( $X_s$ ). To test this assumption,  $X_s$  of a given beat was clamped to the value of  $X_s$  of the preceding beat. Independent of the particular beat where clamping was applied the following behavior was observed: 1) S:R pattern always progressed to S+1:R+1 pattern and 2) the superimposed action potentials of the two beats with the same  $X_s$  overlapped because of equal time latency from stimulus to response. An example of this procedure is shown in Figure 17 for an initial

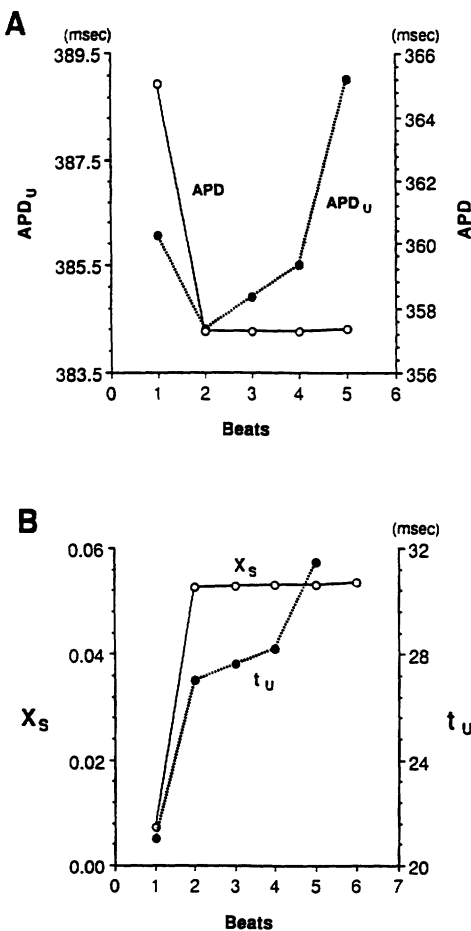


FIGURE 18.  $APD_U$ ,  $APD$ ,  $X_s$ , and  $t_u$  for the 6:5 pattern are plotted as a function of beat number. Panel A: Nonmonotonic behavior of  $APD$  and  $APD_U$ . Panel B: Monotonic increase in  $X_s$  and  $t_u$ .  $APD_U$ , action potential duration from onset of stimulation to 90% repolarization;  $APD$ , action potential duration from maximum upstroke velocity to 90% repolarization;  $X_s$ , activation gate of the time-dependent potassium current at onset of stimulation;  $t_u$ , latency from onset of stimulation to maximum upstroke velocity.

S:R=6:5 (see Figure 16A). The  $X_s$  of the fourth beat was clamped to the  $X_s$  of the third beat. The pattern (Figure 17A) has changed to S:R=7:6 because of resetting of the fourth beat to the third beat. When the action potentials are superimposed (Figure 17B) by setting time zero at the onset of each stimulus, the action potential of the clamped beat overlaps with the previous action potential (i.e.,  $t_u$  and  $APD$  [defined in Figure 5] have the same values for the two beats). Also, when  $X_s$  for all beats is clamped to  $X_s$  of the first beat (not shown) S:R is always 1:1. Clearly,  $X_s$  plays a dominant role in determining the pattern of Wenckebach periodicity.

To further elucidate the mechanism through which the  $I_K$   $X$  gate controls the activation pattern, we plotted  $APD$ ,  $APD_U$ ,  $t_u$  (see Figure 5 for definitions), and  $X_s$  as a function of beat number (Figure 18). The periodic 6:5 pattern discussed above was used as an

example. Beat 1 in the figure refers to the first beat after activation failure during the previous period. The  $APD_U$  of the second beat ( $APD_{U2}$ ) is smaller than the  $APD_U$  of the first beat ( $APD_{U1}$ ). This is due to a larger decrease (7.7 msec) in  $APD$  than the increase (6 msec) of  $t_u$  from the first beat to the second beat (note  $APD_U = APD + t_u$ ). The relatively large decrease of  $APD$  from beat 1 to beat 2 reflects the twice-longer recovery time before beat 1 that results in a long  $APD_1$  (arrow b in Figure 15) as compared with  $APD_2$  (arrow a in Figure 15). Also, a corresponding large increase in  $X_s$  is observed. Starting from beat 2,  $APD_U$  and  $t_u$  increase monotonically, whereas  $APD$  remains almost constant and  $X_s$  increases very slowly. The monotonic increase in  $APD_U$  implies a progressively shorter recovery time between beats starting from beat 2. As a result,  $X$  is progressively less deactivated at the time of the stimulation ( $X_s$  increases monotonically), until failure occurs. When we set  $X_s$  for all beats equal to  $X_s$  of the first beat, activation failure does not occur and the pattern is always 1:1. This mechanism is consistent with the explanation of Delmar et al.<sup>28</sup>

A deviation from this behavior is observed for the first two beats (Figure 18).  $APD_U$  decreases from beat 1 to beat 2, implying a longer recovery time before beat 3 than before beat 2. However, in spite of the longer recovery time before beat 3,  $X_{S3}$  is greater than  $X_{S2}$ . This seemingly anomalous behavior results from the very different initial conditions at the onset of beats 1 and 2. Beat 1 occurs at an interval of  $2 \cdot BCL$  from the last successful beat of the previous period, implying a much longer (about twice) recovery time than that for all other beats. As a result,  $X$  is almost completely deactivated at the onset of beat 1 ( $X_{S1}=0.007$ ), reaching a maximum value of 0.4215 at plateau potentials. At the onset of beat 2, because of much shorter recovery time,  $X$  is much less deactivated ( $X_{S2}=0.0527$ ), reaching a maximum value of 0.4262 during this beat. The larger maximum value of  $X$  at plateau potentials more than compensates for the increase in recovery time, resulting in  $X_{S3}>X_{S2}$  ( $X_{S3}=0.0529$ ). Hence, in spite of an initial decrease in  $APD_U$ ,  $X_s$  increases monotonically from beat to beat until failure occurs. It should be mentioned that the “anomalous” decrease in  $APD_U$  from beat 1 to beat 2 is not always observed. When stimulating, for the same S:R pattern, at longer BCLs (and therefore with lower stimulus strength) we observe a monotonic increase in  $APD_U$  for all beats, similar to the observations of Delmar et al.<sup>28</sup> This is because as BCL becomes progressively longer (relative to  $\tau_x$ ), the change in  $X_s$  from beat 1 to beat 2 becomes progressively smaller, resulting in a smaller decrease of  $APD$  until  $APD$  approaches a constant value. In contrast, for a given S:R pattern, the increase of  $t_u$  from beat 1 to beat 2 remains in the range of 5.5–7 msec for all BCLs (obviously, to keep the same S:R pattern the stimulus strength was adjusted for different BCLs). Because  $APD_U = APD + t_u$ ,  $APD_U$  in-

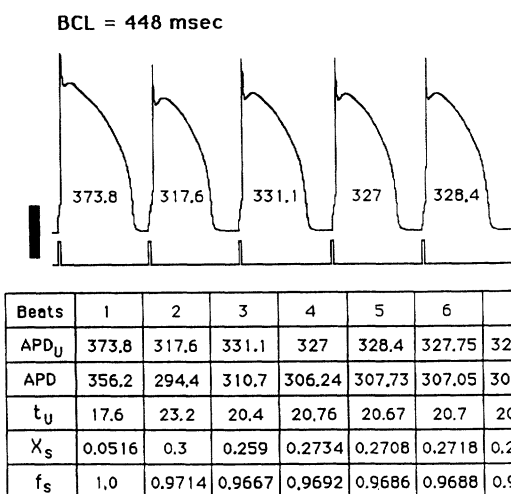


FIGURE 19. Beat-to-beat alternans at short basic cycle length (BCL, 448 msec). Numbers inside action potentials are values of APD<sub>U</sub>. Values of APD<sub>U</sub>, APD, t<sub>U</sub>, X<sub>S</sub>, and f<sub>S</sub> are depicted in the table. APD<sub>U</sub>, APD, and t<sub>U</sub> are in milliseconds, whereas X<sub>S</sub> and f<sub>S</sub> are dimensionless. APD<sub>U</sub>, action potential duration from onset of stimulation to 90% repolarization; APD, action potential duration from maximum upstroke velocity to 90% repolarization; X<sub>S</sub>, activation gate of the time-dependent potassium current at onset of stimulation; t<sub>U</sub>, latency from onset of stimulation to maximum upstroke velocity; f<sub>S</sub>, inactivation gate of the slow inward current at onset of stimulation. Calibration bar, 35 mV.

creases from beat 1 to beat 2 for long BCLs, resulting in a monotonic behavior throughout the period.

The staircase of Figure 16B is shifted toward shorter BCLs when the stimulus strength is increased. In particular, the transition from the 1:1 pattern to the 2:1 pattern is obtained at BCL=448 msec (rather than 882 msec) when the stimulus strength is increased to 3.34  $\mu$ A. The transition from 1:1 to 2:1 at shorter BCLs is preceded by alternans in APD<sub>U</sub> as BCL is decreased in the range of 1:1 response, approaching the transition to 2:1. APD<sub>U</sub> for consecutive beats together with the initial values of the I<sub>K</sub> X gate and the I<sub>si</sub> f gate are shown in Figure 19. Clearly, the alternans in APD<sub>U</sub> result from alternating kinetics of both the I<sub>K</sub> and I<sub>si</sub> channels. When f and X at the time of stimulus for all beats are set equal to their values at the first beat, no alternans are observed. When only the f gate is clamped as above, the transition from the 1:1 pattern to the 2:1 pattern still occurs; however, the number of alternating beats is decreased (four instead of seven), and the amplitude of the APD<sub>U</sub> changes is reduced. In contrast, when only the X gate is clamped, the 1:1 pattern is maintained and no transition from the 1:1 to 2:1 pattern is observed, indicative of the dominant role of I<sub>K</sub> in determining the response to repetitive stimulation at all values of BCL. Alternans in APD<sub>U</sub> are still observed; however, their number is reduced to four beats, and the amplitude of the APD<sub>U</sub> changes is greatly diminished.

The simulations described above identify the ionic channel kinetics responsible for the alternans phenomenon. It remains to be clarified why these alternans appear only for short BCLs (BCL<560 msec in our simulations). Under these conditions (the example we show is for BCL=448 msec) we observe a relatively large decrease (56.2 msec) in APD<sub>U</sub> from beat 1 to beat 2 that reflects a large decrease (61.8 msec) in APD. The large change in APD is possible because short BCL corresponds to the steep portion of the APD restitution curve (Figure 15). Mechanistically, the large APD change results from a relatively large increase in X gate and a decrease in f gate (Figure 19). This decrease in APD<sub>U</sub> is followed by a long recovery time of 130.4 msec to the third beat. This recovery time is long enough so that the X gate at the onset of beat 3 is relatively more deactivated in spite of its large initial value at the onset of beat 2, bringing about an increase in APD<sub>U</sub> of beat 3. The following recovery time is therefore decreased, resulting in a decrease in APD<sub>U</sub> of beat 4. This alternating pattern continues until a stable steady state is achieved with a constant APD<sub>U</sub>=327.66 msec. In contrast, for BCL>700 msec, the changes in APD<sub>U</sub> are smaller (<23 msec) since this range corresponds to the flat portion of the APD restitution curve (Figure 15). Therefore, the decrease in APD<sub>U</sub> from beat 1 to beat 2 results in a relatively small increase in the recovery time to beat 3. This recovery time is too small to compensate for the large initial value of X at the onset of beat 2. As a result, X<sub>S</sub> increases monotonically from beat to beat and no alternans are observed.

It should be emphasized that the large changes in APD<sub>U</sub> at short BCL reflect large changes in APD. This is because at short BCL the stimuli are applied during a fast-recovery phase of the APD restitution curve (Figure 15). In contrast, for long BCL, the stimuli are applied during a slow phase of the restitution curve (Figure 15), resulting in small changes in APD. Consequently, for long BCL, APD<sub>U</sub> changes are determined by changes in t<sub>U</sub> (except for beat 1 to beat 2, where APD also changes significantly as described above). Starting from beat 2 changes in APD<sub>U</sub> are determined by t<sub>U</sub> alone (since APD approaches a constant value). As shown in Figure 18, the increase in t<sub>U</sub> starting from beat 2 results in a monotonic increase in APD<sub>U</sub> and a progressively shorter recovery time between beats until activation failure occurs. The result of this progressive decrease in membrane excitability is the appearance of non-integer S:R patterns (such as 8:7, 7:6, 6:5, etc.) between 1:1 and 2:1 and all other integer S:R ratios. These noninteger S:R patterns are observed over a BCL interval of 2 msec. In contrast, for short BCL, noninteger S:R patterns are not observed in our simulations and there is a direct transition from 1:1 to 2:1 (and between all other integer S:R ratios). This is because for short BCL APD<sub>U</sub> changes are dominated by the large changes in APD (and not by t<sub>U</sub>). Under these conditions, the recovery time does

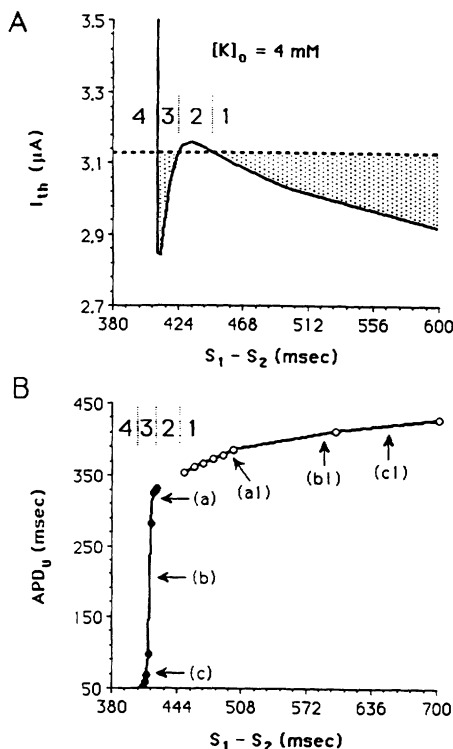


FIGURE 20. Strength-interval curve (panel A) and  $APD_U$  restitution curve (panel B) for  $[K]_o=4 \text{ mM}$ . In panel A horizontal dotted line indicates the stimulus amplitude used in this simulation. Excitable regions (1 and 3) are shaded to distinguish them from the inexcitable regions (2 and 4). The restitution curve in panel B is discontinuous because of the inexcitable region 2.  $I_{th}$ , threshold current;  $APD_U$ , action potential duration from onset of stimulation to 90% repolarization. The letters in panel B are defined in the text.

not decrease progressively from beat to beat since the shortest recovery time is between beat 1 and beat 2. This is because  $APD_U$  is determined by APD, and APD of beat 1 is the longest since it occurs after a recovery time of  $2 \cdot BCL$ . Therefore, if activation is successful at beat 2, all subsequent stimuli result in successful responses and a 1:1 pattern is established. As described above, this 1:1 pattern is characterized by alternans in APD. However, if activation failure occurs, it always occurs at beat 2, where recovery time is the shortest. The result is a direct transition from a 1:1 to 2:1 pattern without the possibility for noninteger S:R patterns.

#### Supernormality and Rate-Dependent Activation

The Wenckebach activation patterns discussed above were obtained in the setting of normal extracellular potassium concentration ( $[K]_o > 4.6 \text{ mM}$ ), for which supernormal excitability does not exist. For low extracellular potassium concentration, supernormal excitability appears during or immediately after the action potential repolarization phase (see "Supernormal Excitability"). Since the presence of supernormality modifies the strength-interval curve by

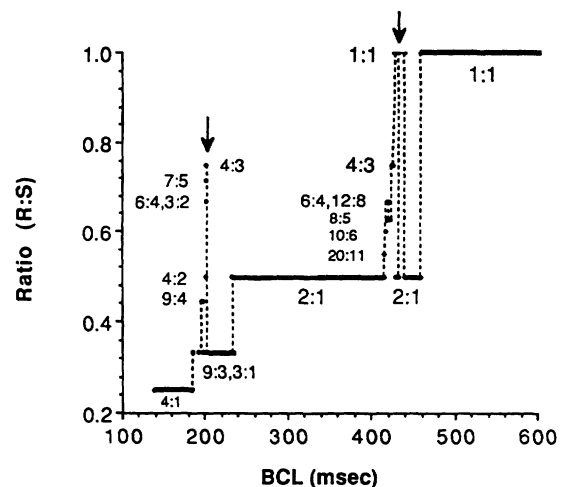


FIGURE 21. Periodic rate-dependent block for low  $[K]_o=4 \text{ mM}$ . Note the nonmonotonic behavior caused by the supernormal phase (arrows). R:S, response-to-stimulus ratio; BCL, basic cycle length. The numbers in the figure indicate the stimulus-to-response ratio, S:R.

introducing nonmonotonic recovery of excitability, we expect rate-dependent activation patterns under conditions of low  $[K]_o$  to be different from the regular rhythms for normal  $[K]_o$  discussed in the previous section. Recently, complex response patterns were observed experimentally by Chialvo et al<sup>7</sup> in Purkinje fibers at low extracellular potassium concentrations ( $[K]_o=4 \text{ mM}$ ). In this section, we will use the L-R model to simulate and investigate this phenomenon.

The strength-interval curve computed for  $[K]_o=4 \text{ mM}$  and a test stimulus of 20-msec duration is plotted in Figure 20A. The horizontal dotted line indicates the current amplitude of the stimuli during repetitive stimulation. For this level of stimulation ( $3.13 \mu\text{A}$ ), four different regions of  $S_1S_2$  interval exist, as characterized by their responses. Regions 1 and 3 are excitable, whereas regions 2 and 4 are inexcitable. Note that excitable and inexcitable regions alternate, so that excitable regions are separated by an inexcitable region. Figure 20B depicts the  $APD_U$  restitution curve for the same conditions. The same four regions are identified. Note the discontinuity of this curve in region 2, corresponding to the inexcitable region in Figure 20A. Also,  $APD_U$  is almost constant in region 1, while in region 3 a fast rate of change is observed. This fast change of  $APD_U$  is caused by the relatively fast decrease of the X gate during this phase (see "Wenckebach Periodicity and Channel Behavior").

The results of a simulated repetitive stimulation experiment with the stimulus strength indicated in Figure 20A (current amplitude of  $3.13 \mu\text{A}$ ) are shown as the staircase plot of the R:S ratio versus BCL of stimulation (Figure 21). Numbers in the figure indicate the S:R ratios. This format is the same as that for Figure 16B, which was obtained for  $[K]_o=5.4 \text{ mM}$ , in the absence of supernormality. A comparison of these figures clearly demonstrates that the activation patterns are different under these two different condi-

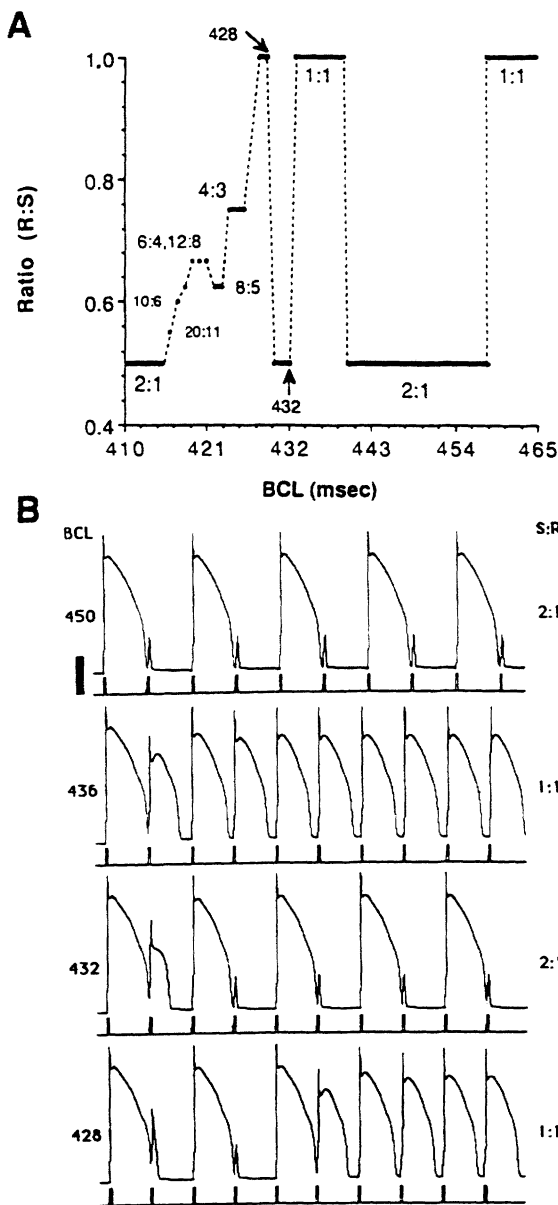


FIGURE 22. The first nonmonotonic range of Figure 21 is enlarged here by showing the range of basic cycle length (BCL) from 465 to 410 msec (panel A). Panel B: Related activation patterns are plotted (calibration bar, 35 mV). R:S, response-to-stimulus ratio; S:R, stimulus-to-response ratio. Numbers in panel A are S:R ratios. Arrows in panel A indicate a specific BCL.

tions. For normal  $[K]_o$  (no supernormality) a monotonic progression of the activation ratio is observed (Figure 16B). In contrast, nonmonotonic changes in the activation ratio are observed for low  $[K]_o$  (supernormality present) (Figure 21). Under these conditions, a stable 1:1 pattern is followed by a region of nonmonotonic behavior as BCL is decreased below 458 msec (right arrow). This nonmonotonic region covers a range of BCLs from 458 to 415 msec. Below 415 msec another regular region of a 2:1 pattern is obtained, followed by another region of nonmono-

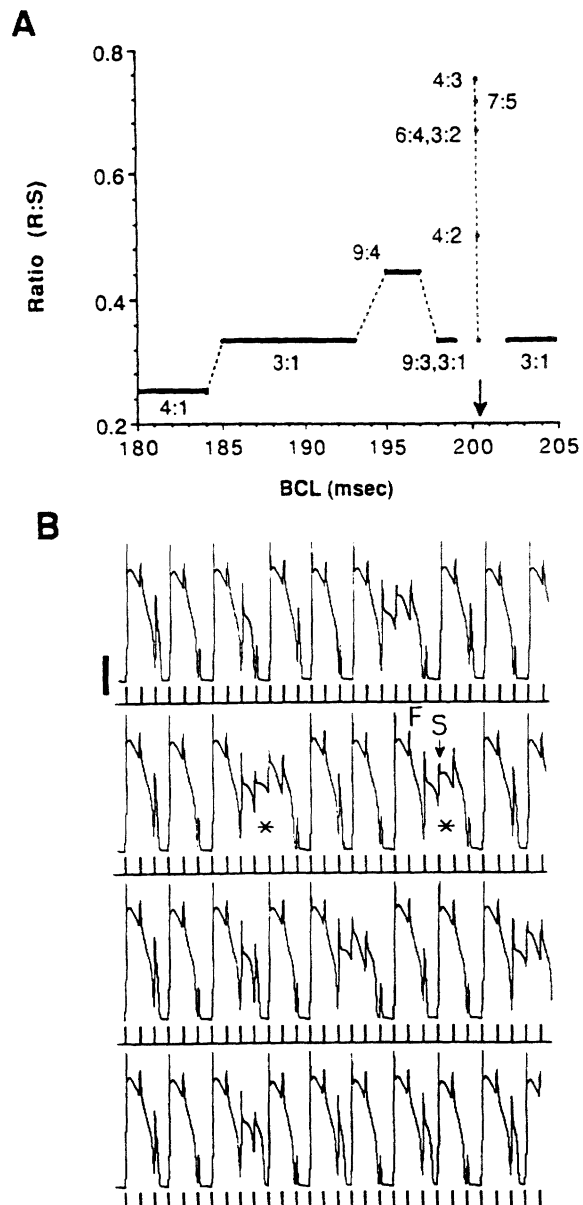


FIGURE 23. The second nonmonotonic range of Figure 21 is enlarged here by showing the range of basic cycle length (BCL) from 205 to 180 msec (panel A). Panel B: Highly aperiodic patterns that correspond to  $BCL = 200.4$  msec (arrow in panel A) are plotted (calibration bar, 35 mV). In the second row of panel B, \* indicates complex patterns of consecutive action potentials; F and S indicate activation failure or success, respectively. R:S, response-to-stimulus ratio. Numbers in panel A are stimulus-to-response (S:R) ratios. For action potentials with rapid sodium-dependent upstroke we define success as peak  $I_{Na}$  greater than 1% of the peak  $I_{Na}$  under fully recovered conditions. For slow response action potentials (upstroke depends on  $I_{si}$ ) we define success as an action potential of duration greater than 50 msec (not including the stimulus duration).

tonic behavior (BCLs from 205 to 190 msec, left arrow). Note that the same patterns repeat for different regions of BCL. For example, a 1:1 pattern is

observed for a BCL of 500, 438, and 428 msec. These regions are separated by regions of 2:1 patterns.

The nonmonotonic regions of Figure 21 are amplified in Figures 22A and 23A. In Figure 22A, as BCL is decreased from 465 msec the activation pattern changes from 1:1 to 2:1 at a BCL of 458 msec and then returns to the 1:1 pattern at a BCL of 439 msec. This nonmonotonic transition from 2:1 to 1:1 is possible because of the nonmonotonic strength-interval curve (supernormality) of Figure 20A. The 2:1 pattern in Figure 22A occurs over a range of BCLs (between 458 and 440 msec) that corresponds to region 2 of the strength-interval curve (Figure 20A). A stimulus at this region fails to elicit a response so that the next stimulus occurs at  $2 \cdot \text{BCL}$  in region 1 of the strength-interval curve, resulting in a successful response. A 2:1 pattern is thus established (see the first row in Figure 22B). The 1:1 pattern of activation for BCLs between 439 and 433 msec is also shown in Figure 22B (second row). The first action potential is of maximum duration because it is stimulated from a fully recovered membrane. The second stimulus is applied during the supernormal phase (region 3 in Figure 20A) and displays a shorter duration. This is because the stimulus is timed during the fast decreasing phase of the restitution curve (point a in Figure 20B). As a result, a longer recovery time follows this action potential and the third stimulus is applied in region 1 of the strength-interval curve (Figure 20A). However, the duration of the third action potential (point a1 in Figure 20B) is still shorter than that of the first action potential, obtained under fully recovered conditions. Consequently, the recovery time is longer and all subsequent stimuli are applied in region 1 of the strength-interval curve, resulting in a 1:1 pattern. For a further decrease in BCL, the pattern returns to 2:1 (BCL of 432 msec), and then back to 1:1 (BCL of 428 msec). These two patterns are shown in Figure 22B (third and fourth rows, respectively). For a BCL of 432 msec, the second action potential is of short duration, corresponding to point b on the restitution curve of Figure 20B (note that the  $\text{APD}_U$  at b is smaller than that at point a). The following stimulus elicits an action potential of duration (b1) on the restitution curve ( $b1 > a1$ ). As a result, the next stimulus is timed during region 2 of the strength-interval curve and does not elicit a successful response. A 2:1 pattern is thus established. For a BCL of 428 msec (see Figure 22B) the second response is of a very short duration, corresponding to point c in Figure 20B. The following stimulus is applied after a long recovery time, resulting in an action potential of long duration (point c1 in Figure 20B). As a result, the next stimulus is applied in region 2 of the strength-interval curve and fails to elicit an action potential. This event is followed by a long recovery time and an action potential of long duration so that the next stimulus is timed during the supernormal phase (region 3) of the strength-interval curve, resulting in a successful response of short duration. After these transitional events the pattern

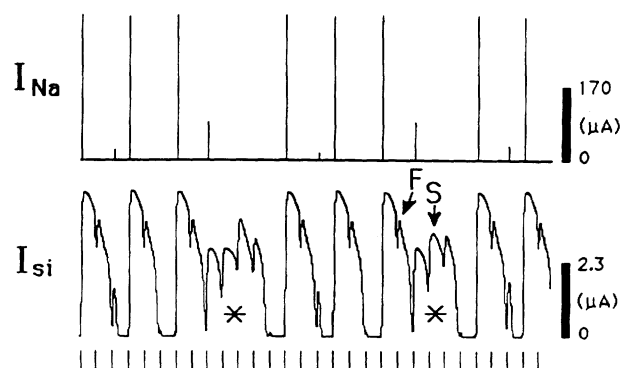


FIGURE 24. Sodium current ( $I_{Na}$ , upper panel) and calcium current ( $I_{si}$ , lower panel) underlying the highly aperiodic patterns in the second row of Figure 23B. Note that the activation success indicated by S results from a slow response that does not involve the sodium current. F, activation failure; \*, complex patterns of  $I_{si}$  that correspond to the complex patterns of action potentials in Figure 23B. Calibration bars, 35 mV. For action potentials with rapid sodium-dependent upstroke we define success as peak  $I_{Na}$  greater than 1% of the peak  $I_{Na}$  under fully recovered conditions. For slow response action potentials (upstroke depends on  $I_{si}$ ) we define success as an action potential of duration greater than 50 msec (not including the stimulus duration).

is similar to that obtained for a BCL of 436 msec (see Figure 22B), and a ratio of 1:1 is established. A similar interplay between the excitability and APD at the different regions defined in Figures 20A and 20B determines the various patterns as BCL is further decreased.

In Figure 23A, as the BCL is reduced below 205 msec, irregular activation patterns are observed. An example is shown in Figure 23B for a BCL of 200.4 msec (arrow in panel A). For this particular BCL, unstable patterns are observed and no regular periodicity is established for more than 250 consecutive stimuli. This behavior is consistent with the experimental findings of Chialvo et al,<sup>7</sup> who observed highly aperiodic activity (termed "chaotic activity") at a BCL of 200 msec with no repeated patterns for recording periods that encompassed 100 or more stimuli. In our simulations, after a transient chaotic pattern that lasted more than 250 consecutive stimuli a very complex pattern with very long periodicity of about 13 seconds (67 stimuli) was established.

The highly aperiodic activity occurs at a BCL below 205 msec. For this range of BCL, the stimuli are frequently applied during region 3 of the strength-interval curve (supernormal phase). In this region, the APD depends very strongly on the time of stimulation. In fact,  $\text{APD}_U$  changes by 281 msec over an  $S_1S_2$  interval of 15 msec (Figure 20B). As a result, a small change in the time of stimulation during the supernormal phase can cause a very large change in the duration of the elicited action potential and in the timing of the next stimulus. Consequently, small variations in the time of stimulation in region 3 can shift the timing of the next stimulus between different

regions of the strength-interval curve, eliciting a very different response. This high sensitivity to the timing of stimulation ("initial conditions") is the basis for the unstable patterns ("chaotic activity"). It should be noted that at a BCL between 410 and 465 msec nonmonotonic behavior of the activation patterns is also observed. However, for this range of BCL there are no unstable patterns or aperiodic activity. This is because for the longer BCL, the stimuli are infrequently applied during region 3 of the strength-interval curve (supernormal phase). Moreover, a stimulus during region 3 is never followed by another stimulus in the same region. The next stimulus always falls either in region 2 (activation failure) or in region 1 (the flat portion of the restitution curve, Figure 20B). On the flat portion of the restitution curve, small changes in the time of the stimulation can cause only very small changes in APD. This has a stabilizing effect on the response so that irregular activity and unstable patterns do not occur.

To further elucidate the ionic current behavior during the highly aperiodic activity, in Figure 24 we plotted the magnitude of  $I_{Na}$  and  $I_{si}$  that corresponds to the pattern shown in Figure 23B, second row from the top. An important observation is that most of the responses during the complex patterns do not involve the fast sodium channel and depolarization is caused by  $I_{si}$ . In Figure 23B, F identifies an activation failure during the plateau of an action potential that was initiated in region 1 of the strength-interval curve. A successful activation during the plateau of an action potential that was initiated in region 3 of the strength-interval curve is identified by S in the figure. The corresponding events in the  $I_{si}$  curve are also identified by F and S, respectively (Figure 24). The difference between the peak magnitudes of  $I_{si}$  for these two events is very small (0.2  $\mu$ A). However, the total outward current ( $I_{K1(T)} + I_K$ ) at F is 3.93  $\mu$ A as compared with only 2.35  $\mu$ A at S. This decrease is mostly due to reduced  $I_{K1(T)}$  at the lower membrane potential of S and results in a successful response, bringing about a very complex pattern of activation. It should be mentioned that this behavior involves the negative slope characteristic of the  $I_{K1(T)}$  curve (Figure 3). When we eliminate the negative slope in the  $I_{K1(T)}$  curve (not shown), unstable patterns do not appear.

### Discussion

The goal of this study is to construct a model of the membrane action potential of the mammalian ventricular cell based, whenever possible, on recent experimental findings in single-cell and single-channel studies. In this report we reformulate three ionic currents:  $I_{Na}$ ,  $I_K$ , and  $I_{K1(T)}$ .  $I_{Na}$  is inactivated by two processes—fast and slow. The slow process of inactivation also implies slow recovery of excitability. In addition,  $I_{Na}$  is characterized by a large channel conductance resulting in fast upstroke velocity ( $V_{max}=400$  V/sec) of the action potential. A newly discovered potassium channel that activates at high potentials is implemented as a component of  $I_{K1(T)}$  in

the model.  $[K]_o$  dependence of  $I_K$  and  $I_{K1(T)}$  is a major feature of the model. This enables us to simulate various phenomena that involve changes in  $[K]_o$ . In this paper we focus on the rising phase, the late repolarization phase, and the postrepolarization phase of the action potential. We use the model to investigate phenomena that involve  $I_{Na}$ ,  $I_K$ , and  $I_{K1(T)}$  during these phases such as supernormal excitability, membrane responsiveness, and Wenckebach periodicity. The results are consistent with the experimental observations, and the phenomena are well described in terms of ionic channel behavior. It should be emphasized that the present model does not include ionic pumps and exchange mechanisms. It therefore cannot simulate dynamic changes in ionic concentrations. The slow inward current in the model is adopted from the B-R model and is not consistent with recent findings related to calcium currents through the membrane such as the existence of two types of calcium channels, L and T, and the role played by  $[Ca]_i$  in inactivation. Also, while an uptake mechanism of intracellular calcium is represented in the model, the model cannot simulate intracellular calcium transients that result from the interaction between calcium currents through the sarcolemma and calcium release and uptake by the sarcoplasmic reticulum. A second phase of the ventricular model presented here is currently being developed in our laboratory to include all of these processes based on recent experimental data. Such processes were first incorporated in a model of the Purkinje action potential by DiFrancesco and Noble<sup>5</sup> in 1985.

We use the Hodgkin-Huxley formalism to describe the macroscopic (ensemble) behavior of ionic channels. This choice is consistent with (and dictated by) our goal, namely, the reconstruction of the membrane action potential that results from ensemble currents through many individual channels. However, one should practice caution when extrapolating from the ensemble behavior to the single-channel behavior, especially when the cardiac sodium channel kinetics are considered. While many single sodium channel properties correspond to similar characteristics of the ensemble current<sup>43,44</sup> and are adequately described by the Hodgkin-Huxley kinetics, some properties are not. For example, at potentials near threshold for sodium channel activation, both channel activation and inactivation determine the kinetics of the macroscopic sodium current decay (i.e., current inactivation).<sup>44,45</sup> The microscopic behavior of ionic channels other than the sodium channels can be adequately described by the Hodgkin-Huxley kinetics.<sup>26,30</sup>

For the sake of clarity, the discussion below is divided into modeling aspects and physiological simulation aspects of the study.

### Modeling Considerations

$I_{Na}$ : Fast sodium current. The fast upstroke velocity of the action potential has been measured in single cells.<sup>13,46,47</sup> The  $V_{max}$  measured by Brown et al<sup>13</sup> is in

the range of 200–300 V/sec at 20–22°C. By applying a minimum  $Q_{10}$  of 1.23,<sup>48</sup>  $V_{max}$  is at least 272–410 V/sec at 37°C.  $V_{max}$  of the E-J model is 300 V/sec, while it is 400 V/sec if computed by the L-R model. The faster upstroke in the L-R model results from adjusting the reversal potential from 29 mV (E-J model) to 54.4 mV to reflect the different intracellular sodium concentration in mammals ( $[Na]_i=18$  mM)<sup>13,23</sup> and chicken embryos ( $[Na]_i=40$  mM).<sup>25</sup> This adjustment gives  $V_{max}=400$  V/sec in the range of measured values. It also results in an overshoot (41.7 mV) of the action potential that is in good agreement with the experimental findings in guinea pig ventricular cells.<sup>31,35</sup>

A tetrodotoxin (TTX)-sensitive slow sodium current that affects the action potential duration has been identified in single-channel recordings.<sup>49–52</sup> In guinea pig ventricular cells, a low dose of TTX ( $\leq 30$   $\mu$ M) does not affect the APD significantly.<sup>35,53</sup> However, Kiyosue and Arita,<sup>52</sup> using a high dose of TTX (60  $\mu$ M), observed ~10% shortening of the APD. This slow current is different from the window current caused by the overlap of the  $m^3$  and  $h_\infty$  curves at high potentials,<sup>51,52</sup> as demonstrated by the fact that TTX can affect the APD with little (or no) change in  $V_{max}$ .<sup>9,54</sup> The kinetics of this slow current are still not completely elucidated, and it is not included in the L-R model. We will have to include this channel in future studies (as more data become available), especially if effects of drugs are to be studied (some local anesthetics can affect this current).

Two time constants (fast and slow) better describe the inactivation of the sodium channel.<sup>13,49,50,55,56</sup> This cannot be described by the Hodgkin-Huxley kinetics with one inactivation gate. Similar to Beeler and Reuter we incorporated two Hodgkin-Huxley-type inactivation gates as suggested by Haas et al.<sup>24</sup> Haas et al<sup>24</sup> proposed that two inactivation gates ( $h$  and  $j$  in the L-R model) with different time constants can describe the macroscopic behavior of the sodium current inactivation. Following this strategy, the L-R model correctly simulated the behavior of the sodium channel observed experimentally (Figures 7 and 8). Without slow recovery from inactivation (a property not included in the E-J model or in the DiFrancesco-Noble model)  $I_{Na}$  recovery from inactivation follows the same time course following different periods of inactivation (Figure 7D). This is inconsistent with the experimental observations (Figure 7A) by Ebihara et al.<sup>36</sup> Also, without slow recovery from inactivation, the fast recovery of  $I_{Na}$  results in an unrealistically fast recovery of excitability at a high level of membrane potential during the repolarization phase of an action potential (Figure 8D). Note that a conservative value of  $\tau_j$  was used in our simulations. We used a maximum  $\tau_j$  of ~80 msec at  $V=-65$  mV. Values as high as 200 msec were reported in the literature.<sup>14</sup>

To account for this process of slow recovery from inactivation, alternative models to that of Hodgkin and Huxley were proposed to describe an inactivation gate with two time constants (fast and slow).

Chiu<sup>57</sup> proposed a modified Hodgkin-Huxley formalism (second-order kinetics) to describe two processes of inactivation. However, Brown et al<sup>13</sup> found that the  $h_\infty(V)$  curve can be described by a single exponential, a result that is also supported by the recent observations for single-channel recordings.<sup>44</sup> This deviates from the prediction of Chiu's model<sup>57</sup> that  $h_\infty$  has to be described by two exponentials as a function of voltage. Recently, Markov chain models have been proposed to describe the sodium channel kinetics in cardiac cells.<sup>58</sup> Based on single-channel recordings and a five-state Markov model,<sup>59</sup> Scanley et al<sup>45</sup> provided a kinetic analysis of the sodium channel. The basic five-state model reproduced observed open-duration data and reopening behavior but produced only a single exponential decay of current, implying that more complex models are required.

Single-channel recordings demonstrate that near-threshold potentials for channel activation sodium channels tend to open more than once during a depolarization (reopening phenomenon<sup>44,45</sup>). Also, a significant fraction of sodium channels do not open by the time of peak inward current. These microscopic phenomena determine the time course of the macroscopic current decay and provide the basis for the slow macroscopic current inactivation that is introduced in our model by the  $j$  gate.

$I_K$ : Time-dependent potassium current. The formulation of  $I_K$  in our model is based on the form suggested by Shibasaki<sup>26</sup> to fit his data in nodal cells, but its parameters are obtained from the B-R model of the ventricular action potential. Note that the property of  $[K]_o$ -dependent activation is introduced as a square root dependence of the maximum conductance. In contrast, the DiFrancesco-Noble formulation<sup>5</sup> results in a linear dependence of channel conductance on  $[K]_o$  in the physiological range of  $[K]_o$  from 2 to 10 mM. The simulated results (Figure 1) are consistent with the experimental findings by McDonald and Trautwein<sup>29</sup> and Shibasaki<sup>26</sup> and include minimal crossover between current-voltage curves of different  $[K]_o$  and strong inward rectification. An alternative formulation could be constructed from the data measured by Matsuura et al<sup>27</sup> in guinea pig single ventricular cells. They measured the fully activated  $I_K$  curve [ $\bar{I}_K(V)$ ] for  $[K]_o=5.4$  mM and proposed that  $I_K=\bar{I}_K \cdot X^2$  ( $I_K$  activation is proportional to the second power of the activation gate,  $X$ ). We introduced  $[K]_o$  dependence in their formulation and investigated the behavior of  $I_K$  for different values of  $[K]_o$ . The results displayed significant crossover between  $\bar{I}_K$  curves of different  $[K]_o$ . This is inconsistent with the experimental observations.<sup>26,29</sup> We then introduced this alternative formulation of  $I_K$  in the L-R model of the action potential. Since the surface membrane area was not given by Matsuura et al,<sup>27</sup> we adjusted the maximum conductance ( $\bar{G}_K$ ) based on the mean capacitive membrane area measured by Isenberg and Klöckner ( $2 \times 10^{-4}$  cm<sup>2</sup>/cell)<sup>31</sup> and Kamp et al ( $8.52 \times 10^{-5}$  cm<sup>2</sup>/cell).<sup>60</sup> This resulted

in  $\bar{G}_K=0.143 \text{ mS/cm}^2$  and  $\bar{G}_K=0.335 \text{ mS/cm}^2$ , respectively, in comparison with the L-R  $\bar{G}_K=0.282 \text{ mS/cm}^2$ . Note that specific capacitance of  $1 \mu\text{F/cm}^2$  is assumed. The (adjusted) alternative  $I_K$  failed to repolarize the membrane when  $[K]_o \leq 4.5 \text{ mM}$  (for  $\bar{G}_K=0.143 \text{ mS/cm}^2$ ) and  $[K]_o \leq 2.2 \text{ mM}$  (for  $\bar{G}_K=0.335 \text{ mS/cm}^2$ ), and the membrane potential stayed at about  $-30$  to  $-40 \text{ mV}$ . This is inconsistent with the experimental observations at low  $[K]_o$ . Tseng et al<sup>9</sup> observed repolarization at  $[K]_o=2 \text{ mM}$  but not at  $[K]_o=1 \text{ mM}$ . This behavior is simulated correctly by the L-R  $I_K$  in spite of its smaller conductance ( $\bar{G}_K < 0.335 \text{ mS/cm}^2$ ). This inability of the Matsuura et al<sup>27</sup>  $I_K$  to repolarize the membrane in spite of the large conductance results from the  $X^2$  dependence of  $I_K$ . For these reasons we formulated the L-R  $I_K$  to depend on  $X$  (rather than  $X^2$ ), as suggested by Shibasaki.<sup>26</sup> It should be emphasized, however, that the behavior of  $I_K$  was demonstrated in a model that retains the slow inward current formulation of the B-R model. The Matsuura  $I_K$  will have to be reexamined once an accurate model of  $I_{Ca}$  is developed.

$I_{K1(T)}$ : Total time-independent potassium current. This current is equivalent to  $I_{K1}$  in the B-R model<sup>3</sup> and is renamed here  $I_{K1(T)}$  based on the following recent findings. In single-channel recordings, Kurachi<sup>30</sup> found that 1) an inactivation gate (K1) of  $I_{K1}$  is a function of membrane potential and of the potassium Nernst potential and 2) this gate completely inactivates at plateau potentials, resulting in zero  $I_{K1}$  current at these potentials. The zero contribution of  $I_{K1}$  at plateau potentials was also observed by Isenberg<sup>32</sup> and Shah et al.<sup>34</sup> Therefore, the total (non-zero) time-independent potassium current ( $I_{K1(T)}$ ) at high (plateau) potentials must result from current through other channels. Kakei et al<sup>61</sup> and Iijima and Taira<sup>62</sup> found that the shortening of the APD caused by potassium channel agonists (nicorandil and pinacidil) is a result of increasing the current only at high potentials. This observation supports the Yue and Marban<sup>12</sup> discovery of a plateau potassium channel ( $I_{Kp}$ ) that activates only at high potentials. This channel is characterized by a much smaller time constant than  $I_K$ , no detectable inactivation for more than 600 msec, and high selectivity to potassium ions. Also, the maximum conductance ( $\bar{G}_{Kp}$ ) is largely insensitive to changes in  $[K]_o$ . This insensitivity is consistent with the experimental observations by Isenberg and Klöckner (Figure 8 of Reference 8), Sakmann and Trube (Figure 4A of Reference 11), and Tseng et al (Figure 2A of Reference 9) in whole-cell recordings. They observed that the current-voltage curves of  $I_{K1(T)}$  for different values of  $[K]_o$  (1–22 mM) overlap at high potentials. This overlap implies that the plateau currents are insensitive to changes in  $[K]_o$ . According to the observations described above,  $I_{K1}$  contributes no current at plateau potentials and  $I_{Kp}$  can be treated as a component of  $I_{K1(T)}$  that is activated only at plateau potentials. Also, a background current ( $I_b$ ) exists at negative potentials after blocking  $I_{K1}$ .<sup>32–34</sup> Therefore,

$I_{K1(T)}$  consists of at least three currents ( $I_{K1}$ ,  $I_{Kp}$ , and  $I_b$ ). We represent the  $I_{K1(T)}$  as the sum of these three currents to fit the data measured by Sakmann and Trube (Figure 4A of Reference 11) and obtain an excellent fit for all values of  $[K]_o$  (Figure 3). It is of interest to note that the negative slope of the simulated  $I_{K1(T)}$  is smaller than that measured by Kurachi<sup>30</sup> in single-channel recordings. However, the L-R result is consistent with the experimental observations in multicellular<sup>32,63</sup> and single-cell<sup>8,9,34</sup> recordings. Note that the property of  $[K]_o$ -dependent activation is introduced as a square root dependence of the maximum conductance.<sup>10,11</sup> This behavior is different from the linear dependence on  $[K]_o$  over the physiological range in the DiFrancesco-Noble formulation ( $[K]_c < < K_{m,1}$  in their Equation 13).<sup>5</sup>

#### Physiological Simulations

**Membrane response to premature stimulation.** Premature stimulation can be used to investigate the recovery of membrane excitability during the repolarization phase of an action potential. The simulations show that the premature membrane response, indicated by  $\dot{V}_{max}$  measured in mammalian ventricular cells,<sup>14</sup> is well represented by the L-R model (Figure 8). We define the absolute refractory period as the range of membrane potential for which stimulation will result in  $\dot{V}_{max}$  that is smaller than 20% of the fully recovered  $V_{max}$ . The result ( $V > -78 \text{ mV}$ ) of the L-R model (Figure 8B) that incorporates the process of slow recovery from inactivation is very close to the experimental data ( $> -76 \text{ mV}$ , Figure 8A). In the absence of slow recovery from inactivation (E-J model, Figure 8D), the simulation result ( $V > -69 \text{ mV}$ ) deviates significantly from the experimental data. Similar behavior is expected from all models of the sodium channel that do not incorporate the process of slow recovery from inactivation (e.g., Drouhard and Roberge<sup>64</sup>). This comparison demonstrates the importance of the process of slow recovery from inactivation in determining the time course of recovery of membrane excitability during repolarization. Since during repolarization  $j$  is almost completely inactivated and since  $\tau_j >> \tau_h$ , it follows that the membrane responsiveness is controlled by the slow inactivation  $j$  gate. Our simulations also demonstrate the importance of incorporating the correct steady-state characteristics of  $I_{Na}$  inactivation [ $h_z(V)$  and  $j_z(V)$ ] in the model. The steady-state behavior predicted by the B-R model deviates from the experimental behavior of cardiac fibers (compare curve 2 in Figures 8C and 8A), whereas the L-R model (based on the  $I_{Na}$  data from mammalian ventricular cells) simulates the experimental behavior correctly. It is also important to incorporate the correct  $\bar{G}_{Na}$ . The B-R model ( $\bar{G}_{Na}=4 \text{ mS/cm}^2$ ) predicts a  $\dot{V}_{max}$  that is unrealistically slow (115 V/sec), while the L-R model ( $\bar{G}_{Na}=23 \text{ mS/cm}^2$ ) predicts a  $\dot{V}_{max}$  within the range of measured values (400 V/sec). Note that a  $\bar{G}_{Na}$  increase by a factor of almost 6 results in a  $\dot{V}_{max}$  increase by a factor of about 3. This

is because the actual rate of activation of the cardiac sodium channel (represented in the L-R model) is slower than the rate of activation used in the B-R model (modified from squid-axon data). The unrealistic low  $\bar{G}_{Na}$  of the B-R model also leads to an unrealistically long latency from threshold potential to  $\dot{V}_{max}$  (Figure 6D) that is inconsistent with the experimental findings.<sup>28</sup>

So far, we have considered the membrane response at a normal  $[K]_o$  ( $[K]_o=5.4$  mM). The L-R model allows changes in extracellular potassium concentration to be incorporated. We studied the membrane response to premature stimulation for different  $[K]_o$ . The strength–interval curve is determined by the critical (minimum) strength of test stimuli needed to excite the membrane during the repolarization phase of an action potential. Experimentally, the stimulus strength decreases monotonically with repolarization at normal  $[K]_o$ ; however, supernormal excitability has been identified as an interval in which nonmonotonic behavior of the strength–interval curve occurs at low  $[K]_o$ .<sup>7,39</sup> The results (Figure 9) of the L-R model simulations are consistent with the experimental observations. For  $[K]_o>4.6$  mM, the threshold potential decreases during repolarization at a rate that is faster than the rate of repolarization (Figure 12). As a result, membrane excitability increases monotonically during repolarization. For low  $[K]_o$  ( $[K]_o\leq4.6$  mM) there is a range during late repolarization at which the rate of membrane repolarization is faster than the decrease of threshold potential (Figure 12).<sup>38</sup> This results in a decrease of excitability over this range and, therefore, in a nonmonotonic recovery of membrane excitability (Figure 9). The presence of an interval during which excitability is higher than in the adjacent (previous and following) intervals is known as “supernormality.” At the level of channel kinetics, this behavior is a consequence of different kinetics of slow recovery from inactivation of  $I_{Na}$  at different values of  $[K]_o$ . As  $[K]_o$  decreases from 7 to 3 mM, resting potential (primarily controlled by  $I_{K1}$ ), becomes more negative (from  $-78.2$  to  $-95.5$  mV) so that the time constant of sodium channel recovery, dominated by the slow inactivation  $j$  gate, becomes smaller ( $\tau_j$  decreases from 33 to 7 msec). As a result, the sodium channel recovers earlier in the repolarization phase at a range for which repolarization is faster than the rate of decrease of threshold potential, and a supernormal window is created. The interaction between  $I_{K1}$  and slow recovery from inactivation of  $I_{Na}$  in response to changes in  $[K]_o$  determines the amplitude and width of the window of supernormal excitability (Figure 9). Without the process of slow recovery from inactivation, the sodium channel recovers unrealistically earlier so that supernormality is observed even when  $[K]_o$  is as high as 7 mM (Figure 11A). This is inconsistent with the experimental observations.<sup>7,39</sup>

*Periodic stimulation at normal  $[K]_o$ .* Wenckebach rate-dependent block was originally characterized as a propagation-related process that involves decremental conduction. Wenckebach<sup>65</sup> described this

phenomenon in the atrioventricular node. Wenckebach periodicity was also demonstrated in cardiac tissue that contained a region of depressed conduction separating two regions of normal excitability.<sup>66</sup> Recently, Wenckebach periodicity was demonstrated in a single ventricular cell under periodic stimulation,<sup>6,40</sup> indicating that the phenomenon is an intrinsic property of the cell membrane. Using the L-R model at normal  $[K]_o$  (5.4 mM), we investigated the cellular mechanism of the periodic rate-dependent block. The simulations demonstrate that this process is dominated by the kinetics of the X gate of  $I_K$ . This is because membrane excitability is influenced to a large extent by the loss of charge to the extracellular medium through the  $I_K$  channel during stimuli of relatively long duration (20 msec) (see Figures 13 and 14).

As the BCL of periodic stimulation decreases from 2,000 msec, a monotonic decrease of the R:S ratio is observed (staircase in Figure 16B). In our simulations, noninteger patterns of S:R ratios are observed in the transition interval between integer S:R ratios. For example, noninteger Wenckebach patterns (8:7, 7:6, 6:5, etc.) are found between 1:1 and 2:1 (Figure 16B). These patterns are observed in a very narrow interval of about 2 msec. The fact that these patterns occur over such a narrow time interval might be the reason why these various Wenckebach patterns could not be sustained in single myocyte preparations<sup>28,40</sup> since small perturbations (e.g., in temperature and pipette resistance) can cause large changes relative to the narrow transition range. In multicellular preparations<sup>7,65,66</sup> the transition intervals are longer (up to 100 msec) and stable noninteger Wenckebach patterns are observed.

The appearance of Wenckebach block patterns is related to beat-to-beat changes in APD (measured from  $V_{max}$  to 90% repolarization) and the latency from onset of stimulation to  $\dot{V}_{max}$ . Both parameters are controlled by the degree of  $I_K$  deactivation (kinetics of the X gate). For long BCL (BCL>920 msec), APD of all beats in a Wenckebach pattern remains almost constant (see Figure 15), while the latency increases progressively so that deactivation time (BCL–APD–latency) of the X gate decreases monotonically, bringing about a progressive beat-to-beat decrease of membrane excitability. This process continues until activation failure occurs. This is the typical (classical) Wenckebach rate-dependent block observed in cardiac Purkinje fibers<sup>7</sup> and in single ventricular myocytes.<sup>6,40</sup> When BCL decreases (920 msec≥BCL>700 msec), the pattern of beat-to-beat changes becomes different from the typical behavior described above. APD does not remain constant, and recovery time first increases (from second to third beat) and then decreases monotonically. However, membrane excitability still decreases monotonically from beat to beat until activation failure occurs. This is because the beat-to-beat increase in the value of

the X gate at the time of stimulation more than compensates for the initial increase in recovery time (see Figure 18). This atypical (nonmonotonic) behavior of recovery time can be observed in the data of Delmar et al<sup>6</sup> for stimulation at BCL=910 msec. A careful inspection of Figure 1B in their paper demonstrates that total APD (APD+latency) of the first beat in a Wenckebach pattern is greater than that of the second beat; also, the value of plateau potential is decreased. These experimental findings are consistent with the simulations presented here (Figures 17 and 18).

When BCL further decreases (<560 msec), the increase in the value of the X gate (i.e., degree of  $I_K$  activation) does not compensate for the initial increase in recovery time. As a result, membrane excitability increases at the time of the next stimulus, resulting in an action potential of long duration. This implies a shorter recovery time and lower membrane excitability at the time of the following stimulus, so that the following action potential is of short duration. A pattern of beat-to-beat alternans in APD is thus established. The amplitude of alternans (see Figure 19) decreases monotonically until a stable activation pattern (1:1) with constant APD (smaller than that of the fully recovered action potential) is established. Noninteger Wenckebach patterns cannot be found when alternans occur. This is consistent with the experimental observations (at BCL=430 msec) in isolated rabbit ventricular myocytes.<sup>67</sup> The reason is that both phenomena (noninteger Wenckebach patterns and alternans) cannot occur simultaneously. Alternans occur at small BCL, at a range where there is a strong dependence of APD on the time of stimulation (Figure 15), reflecting a strong dependence of the X gate deactivation on the time of stimulation. At this range, the changes in APD are much larger than changes in the latency from stimulus to  $V_{max}$ , so that the recovery time is determined by APD. Since the first beat is of the longest APD (a fully recovered action potential), the recovery time to the second beat is the shortest and all following stimulations will be successful. Hence, a 1:1 pattern is always established when alternans are present. In contrast, noninteger Wenckebach patterns are established at a range of BCL for which large beat-to-beat changes in the latency from stimulus to  $V_{max}$  and small changes in APD are present. At this range, recovery time is determined by the latency from stimulus to  $V_{max}$ , which increases monotonically from beat to beat. The result is a monotonically decreasing recovery time leading to block. Delmar et al<sup>28</sup> used the B-R model with modified  $I_{K1}$  to investigate the Wenckebach phenomenon for long BCL. The simulated transition interval during which noninteger Wenckebach patterns were observed was longer than 20 msec. With such a long interval, one expects that systematic measurements of Wenckebach patterns in single cells will reveal persistent noninteger ratios. This is inconsistent with experimental observations.<sup>6,28,40</sup>

**Periodic stimulation at low  $[K]_o$ .** The L-R model incorporates the possibility of changing  $[K]_o$ . We studied the effects of changes in  $[K]_o$  on the cell response to periodic stimulation. At low  $[K]_o$  the nonmonotonic behavior of the strength-interval curve (Figure 20A) allows stimuli to excite the membrane during the supernormal phase but not at adjacent (earlier or later) intervals. This discontinuity in excitability together with the high sensitivity of APD to the time of stimulation (Figure 20B) during the supernormal phase brings about nonmonotonic behavior of the R:S curve and unstable activation patterns (Figure 21). This complex behavior was observed experimentally and described in a recent paper by Chialvo et al.<sup>7</sup> For long BCL ( $\geq 410$  msec), stimulation is seldom timed during the supernormal phase. As a result, stable but complex activation patterns are observed (such as 10:6, 12:8, 6:4, and 20:11). Also, the same activation patterns are repeated at different ranges of BCL (nonmonotonic staircase behavior, see Figure 22). For short BCL ( $\leq 205$  msec), stimulation is frequently timed during the supernormal phase. Consequently, highly aperiodic patterns that do not stabilize for more than 250 consecutive stimuli are observed (Figure 23). This is consistent with the experimental findings of Chialvo et al.<sup>7</sup> A very small change in BCL (from 200.4 to 200.7 msec) results in very different patterns, indicating very high sensitivity to initial conditions. The unstable patterns are frequently characterized by successful activations during the early repolarization phase of an action potential. This action potential was initiated by a stimulus applied during the supernormal phase. It is characterized by low plateau potentials, in the range where  $I_{K1(T)}$  exhibits a negative slope. The decrease of  $I_{K1(T)}$  with depolarization at this range results in higher membrane excitability and a possibility of successful activation during the early repolarization phase of an action potential. It should be noted that when we eliminate the negative slope in the current-voltage curve of  $I_{K1(T)}$ , the unstable aperiodic patterns disappear. Also, the successful activation at this range is a "slow response" caused by activation of  $I_{si}$  and not of  $I_{Na}$ . Similar unstable aperiodic patterns were predicted by an analytic (difference-differential) model formulated by Chialvo et al.<sup>7</sup> Their model is based on the relations between excitability, latency, and APD. They show that the appearance of aperiodic patterns is related to the presence of supernormality and to the shape of the APD restitution curve at short diastolic intervals. These observations are consistent with the behavior of our membrane model and, as elucidated by our simulations, reflect both large changes in the state of deactivation of the  $I_K$  channel (X gate) and the negative slope characteristic of  $I_{K1(T)}$ .

In summary, the membrane model developed here correctly simulates various phenomena that result from the interaction of excitation and repolarization. This is an important property of the model since reentrant arrhythmias involve this type of interaction

between head and tail of the reentrant action potential.<sup>17</sup> Another property of the model is the ability to introduce changes in  $[K]_o$ . This is also an important aspect of the model since elevated  $[K]_o$  is an important aspect of ischemia that influences propagation and arrhythmogenesis.

The simulations of membrane response to premature stimulation predict a variety of rate-dependent phenomena. These include Wenckebach periodicity, beat-to-beat alternans of APD, and (because of supernormality at low  $[K]_o$ ) unstable aperiodic response patterns that display high sensitivity to initial conditions. The occurrence of Wenckebach periodicity in our simulations support other observations that this phenomenon is an intrinsic property of single cardiac cells. This observation suggests that the single-cell response under a variety of conditions might play an important role in arrhythmogenesis. The occurrence of beat-to-beat alternans in the simulations is intriguing. Beat-to-beat alternans in APD are a property of reentrant action potentials.<sup>17,68</sup> In a broader sense, electrical alternans are detected in many circumstances that are associated with ventricular fibrillation and, as suggested by Guevara et al.,<sup>67</sup> may reflect the first in a cascade of period-doubling bifurcations that eventually result in chaos, that is, fibrillation.<sup>69</sup> As with Wenckebach periodicity, the observation that alternans can be generated at the level of the single cell points to the possible important role of the single-cell response in arrhythmogenesis. Finally, the appearance of highly aperiodic patterns that are extremely sensitive to initial conditions might also be related to arrhythmogenesis since it implies that short propagation delays ( $\sim 1$  msec) can initiate very different responses in neighboring cells (or multicellular fiber bundles). Note that propagation delays of this magnitude can occur across gap junctions under a very moderate degree of cell-to-cell uncoupling.<sup>15,16</sup> We conclude with a word of caution. The behaviors described above are the responses of isolated cells. In the heart, the behavior of cells is modulated by loading conditions and electrotonic interactions.<sup>70</sup> The response of a cell in an ensemble may, therefore, be different from its intrinsic response. Under conditions of increased cell-to-cell uncoupling the individual response of cells (or of a group of cells, i.e., fiber bundles) may become unmasked, bringing about conditions that favor arrhythmogenesis. Verification of these hypotheses awaits further experimentation in multicellular preparations and simulations in a multicellular model of cardiac tissue.

### Acknowledgments

We would like to thank Dr. Gerald Saidel for his help with the parameter estimation procedure. We also thank Dr. Weilun Quan for very helpful discussions.

### References

- Hodgkin AL, Huxley AF: A quantitative description of membrane current and its application to conduction and excitation in nerve. *J Physiol (Lond)* 1952;117:500–544
- McAllister RE, Noble D, Tsien RW: Reconstruction of the electrical activity of cardiac Purkinje fibres. *J Physiol (Lond)* 1975;251:1–59
- Beeler GW, Reuter H: Reconstruction of the action potential of ventricular myocardial fibres. *J Physiol (Lond)* 1977;268:177–210
- Ebihara L, Johnson EA: Fast sodium current in cardiac muscle: A quantitative description. *Biophys J* 1980;32:779–790
- DiFrancesco D, Noble D: A model of cardiac electrical activity incorporating ionic pumps and concentration changes. *Philos Trans R Soc Lond [Biol]* 1985;307:353–398
- Delmar M, Michaels DC, Jalife J: Slow recovery of excitability and the Wenckebach phenomenon in the single guinea pig ventricular myocyte. *Circ Res* 1989;65:761–774
- Chialvo DR, Michaels DC, Jalife J: Supernormal excitability as a mechanism of chaotic dynamics of activation in cardiac Purkinje fibers. *Circ Res* 1990;66:525–545
- Isenberg G, Klöckner U: Isolated bovine ventricular myocytes: Characterization of the action potential. *Pflugers Arch* 1982;395:19–29
- Tseng GN, Robinson RB, Hoffmann BF: Passive properties and membrane currents of canine ventricular myocytes. *J Gen Physiol* 1987;90:671–701
- Sakmann B, Trube G: Conductance properties of single inwardly rectifying potassium channels in ventricular cells from guinea-pig heart. *J Physiol (Lond)* 1984;347:641–657
- Sakmann B, Trube G: Voltage-dependent inactivation of inward-rectifying single-channel currents in the guinea-pig heart cell membrane. *J Physiol (Lond)* 1984;347:659–683
- Yue DT, Marban E: A novel cardiac potassium channel that is active and conductive at depolarized potentials. *Pflugers Arch* 1988;413:127–133
- Brown AM, Lee KS, Powell T: Sodium currents in single rat heart muscle cells. *J Physiol (Lond)* 1981;318:479–500
- Gettes LS, Reuter H: Slow recovery from inactivation of inward currents in mammalian myocardial fibres. *J Physiol (Lond)* 1974;240:703–724
- Rudy Y, Quan W: A model study of the effects of the discrete cellular structure on electrical propagation in cardiac tissue. *Circ Res* 1987;61:815–823
- Rudy Y, Quan W: The effects of the discrete cellular structure on propagation of excitation in cardiac tissue: A model study, in Sperelakis N, Cole W (eds): *Cell Interactions and Gap Junctions*. Boca Raton, Fla, CRC Press, 1989, pp 123–142
- Quan W, Rudy Y: Unidirectional block and reentry of cardiac excitation: A model study. *Circ Res* 1990;66:367–382
- Rush S, Larsen H: A particular algorithm for solving dynamic membrane equations. *IEEE Trans Biomed Eng* 1978;25:389–392
- Victorri B, Vinet A, Robege FA, Drouhard JP: Numerical integration in the reconstruction of cardiac action potentials using Hodgkin-Huxley-type models. *Comput Biomed Res* 1985;18:10–23
- Moore JW, Ramon F: On numerical integration of the Hodgkin and Huxley equations for a membrane action potential. *J Theor Biol* 1974;45:249–273
- Dennis JE, Gay DM, Welsch RE: An adaptive nonlinear least-squares algorithm. *ACM Trans Math Softw* 1981;7:348–368
- Weidmann S: Electrical constants of trabecular muscle from mammalian heart. *J Physiol (Lond)* 1970;210:1041–1054
- Nilius B: Calcium block of guinea-pig heart sodium channels with and without modification by the piperazinylindole DPI 201-106. *J Physiol (Lond)* 1988;399:537–558
- Haas HG, Kern R, Einwachter HM, Tarr M: Kinetics of Na inactivation in frog atria. *Pflugers Arch* 1971;323:141–157
- Ebihara L, Shigeto N, Liberman M, Johnson EA: The initial inward current in spherical clusters of chick embryonic heart cells. *J Gen Physiol* 1980;75:437–456
- Shibasaki T: Conductance and kinetics of delayed rectifier potassium channels in nodal cells of the rabbit heart. *J Physiol (Lond)* 1987;387:227–250

27. Matsuura H, Ehara T, Imoto Y: An analysis of the delayed outward current in single ventricular cells of the guinea pig. *Pflugers Arch* 1987;410:596–603
28. Delmar M, Glass L, Michaels DC, Jalife J: Ionic basis and analytical solution of the Wenckebach phenomenon in guinea pig ventricular myocytes. *Circ Res* 1989;65:775–788
29. McDonald TF, Trautwein W: The potassium current underlying delayed rectification in cat ventricular muscle. *J Physiol (Lond)* 1978;274:217–246
30. Kurachi Y: Voltage-dependent activation of the inward-rectifier potassium channel in the ventricular cell membrane of guinea-pig heart. *J Physiol (Lond)* 1985;366:365–385
31. Isenberg G, Klöckner U: Calcium tolerant ventricular myocytes prepared by preincubation in a “KB medium.” *Pflugers Arch* 1982;395:6–18
32. Isenberg G: Cardiac Purkinje fibers: Cesium as a tool to block inward rectifying potassium currents. *Pflugers Arch* 1976;365:99–106
33. Hirano Y, Hiraoka M: Changes in  $K^+$  currents induced by  $Ba^{2+}$  in guinea pig ventricular muscles. *Am J Physiol* 1986;251:H24–H33
34. Shah AK, Cohen IS, Datyner NB: Background  $K^+$  current in isolated canine cardiac Purkinje myocytes. *Biophys J* 1987;52:519–525
35. Hume JR, Uehara A: Ionic basis of the different action potential configurations of single guinea-pig atrial and ventricular myocytes. *J Physiol (Lond)* 1985;368:525–544
36. Ebihara L, Shigeto N, Lieberman M, Johnson EA: A note on the reactivation of the fast sodium current in spherical clusters of embryonic chick heart cells. *Biophys J* 1983;42:191–194
37. Hoff HE, Nahum LH: The supernormal period in the mammalian ventricle. *Am J Physiol* 1938;124:591–595
38. Weidmann S: Effects of calcium ions and local anaesthetics on electrical properties of Purkinje fibers. *J Physiol (Lond)* 1955;129:568–582
39. Spear JF, Moore EL: The effect of changes in rate and rhythm on supernormal excitability in the isolated Purkinje system of the dog. *Circulation* 1974;50:1144–1149
40. Guevara MR, Jeandupeux D, Alonso F, Morissette N: Wenckebach rhythms in isolated ventricular heart cells, in Pnevmatikos S, Bountis T, Pnevmatikos S (eds): *Singular Behavior and Nonlinear Dynamics*. London, World Scientific, 1989, vol 2, pp 629–642
41. Elharrar V, Surawicz B: Cycle length effect on restitution of action potential duration in dog cardiac fibers. *Am J Physiol* 1983;244(Heart Circ Physiol 13):H782–H792
42. Robinson RB, Boyden PA, Hoffman BF, Hewett KW: Electrical restitution process in dispersed canine cardiac Purkinje and ventricular cells. *Am J Physiol* 1987;253(Heart Circ Physiol 22):H1018–H1025
43. Yue DT, Lawrence JH, Marban E: Two molecular transitions influence cardiac sodium channel gating. *Science* 1989;244:349–352
44. Berman MF, Camardo JS, Robinson RB, Siegelbaum SA: Single sodium channels from canine ventricular myocytes: Voltage dependence and relative rates of activation and inactivation. *J Physiol (Lond)* 1989;415:503–531
45. Scanley BE, Hanck DA, Chay T, Fozard HA: Kinetic analysis of single sodium channels from canine cardiac Purkinje cells. *J Gen Physiol* 1990;95:411–437
46. Bodewei R, Hering S, Lemke B, Rosenshtraukh LV, Undrovinas AI, Wollenberger A: Characterization of the fast sodium current in isolated rat myocardial cells: Simulation of the clamped membrane potential. *J Physiol (Lond)* 1982;325:301–315
47. Zilberman YI, Timin EN, Bendukidze ZA, Burnashev NA: Patch-voltage-clamp method for measuring fast inward current in single rat heart muscle cells. *Pflugers Arch* 1982;394:150–155
48. Colatsky TJ: Voltage clamp measurements of sodium channel properties in rabbit cardiac Purkinje fibres. *J Physiol (Lond)* 1980;305:215–234
49. Patlak JB, Ortiz M: Slow currents through single sodium channels of the adult rat heart. *J Gen Physiol* 1985;86:89–104
50. Kunze DL, Lacerda AE, Wilson DL, Brown AM: Cardiac Na currents and the inactivating, reopening, and waiting properties of single cardiac Na channel. *J Gen Physiol* 1985;86:691–719
51. Grant AO, Starmer CF: Mechanisms of closure of cardiac sodium channels in rabbit ventricular myocytes: Single-channel analysis. *Circ Res* 1987;60:897–913
52. Kiyosue T, Arita M: Late sodium current and its contribution to action potential configuration in guinea pig ventricular myocytes. *Circ Res* 1989;64:389–397
53. Leblanc N, Hume JR: Sodium current-induced release of calcium from cardiac sarcoplasmic reticulum. *Science* 1990;248:372–376
54. Corabœuf E, Deroubaix E, Coulombe A: Effects of tetrodotoxin on action potentials of the conducting system in the dog heart. *Am J Physiol* 1979;236:H561–H567
55. Makielinski JC, Sheets MF, Hanck DA, January CT, Fozard HA: Sodium current in voltage clamped internally perfused canine cardiac Purkinje cells. *Biophys J* 1987;52:1–11
56. Kirsch GE, Brown AM: Kinetic properties of single sodium channels in rat heart and rat brain. *J Gen Physiol* 1989;93:85–99
57. Chiu SY: Inactivation of sodium channels: Second order kinetics in myelinated nerve. *J Physiol (Lond)* 1977;273:573–596
58. French RJ, Horn R: Sodium channel gating: Models, mimics and modifiers. *Annu Rev Biophys Bioeng* 1983;12:319–356
59. Horn R, Vandenberg CA: Statistical properties of single sodium channels. *J Gen Physiol* 1984;84:505–534
60. Kamp TJ, Sanguineti MC, Miller RJ: Voltage- and use-dependent modulation of cardiac calcium channels by the dihydropyridine (+)-202-791. *Circ Res* 1989;64:338–351
61. Kakei M, Yoshinaga M, Saito K, Tanaka H: The potassium current activated by 2-nicotinamidoethyl nitrate (nicorandil) in single ventricular cells of guinea pigs. *Proc R Soc Lond [Biol]* 1986;229:331–343
62. Iijima T, Taira N: Pinacidil increases the background potassium current in single ventricular cells. *Eur J Pharmacol* 1987;141:139–141
63. Cleemann L, Morad M: Potassium currents in frog ventricular muscle: Evidence from voltage clamp currents and extracellular K accumulation. *J Physiol (Lond)* 1979;286:113–143
64. Drouhard JP, Roberge FA: Revised formulation of the Hodgkin-Huxley representation of the sodium current in cardiac cells. *Comput Biomed Res* 1987;20:333–350
65. Wenckebach KF: Zur Analyse des unregelmässigen intermittierenden Pulses: II. Über den regelmässig intermittierenden Puls. *Z F Klin Med* 1899;37:475–488
66. Jalife J, Moe GK: Excitation, conduction and reflection of impulses in isolated bovine and canine cardiac Purkinje fibers. *Circ Res* 1981;49:233–247
67. Guevara MR, Alonso F, Jeandupeux D, Van Ginneken ACG: Alternans in periodically stimulated isolated ventricular myocytes: Experiment and model, in Goldbeter A (ed): *Cell to Cell Signalling: From Experiments to Theoretical Models*. New York, Academic Press, Inc, 1989, pp 551–563
68. Frame L, Simson M: Oscillations of conduction, action potential duration, and refractoriness. *Circulation* 1988;78:1277–1287
69. Adam DR, Smith JM, Akselrod S, Nyberg S, Powell AO, Cohen RJ: Fluctuations in T-wave morphology and susceptibility to ventricular fibrillation. *J Electrocardiol* 1984;17:209–218
70. Lesh MD, Pring M, Spear JF: Cellular uncoupling can unmask dispersion of action potential duration in ventricular myocardium: A computer modeling study. *Circ Res* 1989;65:1426–1440

**KEY WORDS** • cardiac action potential model • fast sodium channel • potassium channels • supernormality • Wenckebach periodicity • chaotic activity

# Circulation Research

JOURNAL OF THE AMERICAN HEART ASSOCIATION



**A model of the ventricular cardiac action potential. Depolarization, repolarization, and their interaction.**

C H Luo and Y Rudy

*Circ Res.* 1991;68:1501-1526

doi: 10.1161/01.RES.68.6.1501

*Circulation Research* is published by the American Heart Association, 7272 Greenville Avenue, Dallas, TX 75231

Copyright © 1991 American Heart Association, Inc. All rights reserved.

Print ISSN: 0009-7330. Online ISSN: 1524-4571

The online version of this article, along with updated information and services, is located on the World Wide Web at:

<http://circres.ahajournals.org/content/68/6/1501>

**Permissions:** Requests for permissions to reproduce figures, tables, or portions of articles originally published in *Circulation Research* can be obtained via RightsLink, a service of the Copyright Clearance Center, not the Editorial Office. Once the online version of the published article for which permission is being requested is located, click Request Permissions in the middle column of the Web page under Services. Further information about this process is available in the [Permissions and Rights Question and Answer](#) document.

**Reprints:** Information about reprints can be found online at:  
<http://www.lww.com/reprints>

**Subscriptions:** Information about subscribing to *Circulation Research* is online at:  
<http://circres.ahajournals.org//subscriptions/>